

A seasonal and interannual study of the western equatorial Atlantic upper thermocline circulation variability

M. L. Vianna^a and V. V. de Menezes^b

^aInstituto Nacional de Pesquisas Espaciais, CP515, São José dos Campos, SP, Brazil

^bVM Oceânica S/C Ltda, Av. Lisboa 50/51, São José dos Campos, SP, Brazil

We use five years (1995-2000) of blended Topex/Poseidon-ERS2 altimeter-derived upper ocean currents to investigate the observed seasonal and interannual variability of the circulation in the western equatorial Atlantic (15°N-15°S; 70°W-25°W) in the upper thermocline level. We produce a sea surface height field by mapping the Pathfinder collinear sea surface height anomaly data into a $0.25^\circ \times 0.25^\circ$ - 10 day resolution grid, adding at each grid point the annual mean dynamic topography relative to 1000 m, which is obtained from the high resolution ($0.25^\circ \times 0.25^\circ$) 1997 Boyer-Levitus climatology. This climatology is first filtered to conveniently preserve features at a 300 km scale. The circulation field offshore the 1000 m isobath was obtained using a generalization of the standard geostrophic equation at each 10-day time step, which is shown to be valid also on the Equator. Comparisons of the altimeter-derived fields are made against data from PIRATA moorings, CTD and ADCP WOCE Etambot cruise data spanning the Equator. It is shown that the currents derived from surface data correlate better with ADCP-measured subsurface rather than to surface currents. The time evolution of annual and interannual patterns of the circulation field have been obtained by separating the velocity components time series into period bands with a combination of EOF and Multichannel Singular Spectrum Analysis. A double-cored NECC is seen in August-September, with the southern branch related to the NBC retroflexion, while the northern branch is related to northern hemisphere westward flows turning to the southeast. The NECC main core at 5°N presents a meandering pattern west of 30°W which slowly propagates westward at a speed of 1.8 km/day. The north branch of the SEC only appears after July, recirculating water into a meandering EUC. An annual equatorial standing wave pattern confined to 3°N-3°S has been detected possibly being the cause of the EUC meanders and the appearance of open ocean windows for leakage of south Atlantic waters into the north Atlantic and vice-versa. The variability between 5°S-15°S is mostly in the interannual band with a very weak annual cycle. The estimation of the mean and interannual variability of the geostrophic meridional transports across 3°N and 3°S revealed an absolute maximum northward transport of 20 Sv at 3°S during January-March 1997, and a relative maximum southward transport of 10 Sv at 3°N centered in June of the same year.

1. INTRODUCTION

In the past few years it has become a consensus that the issue of seasonal, interannual and decadal climate predictability is of importance for global economic and social issues. At

these time scales, the ocean-atmosphere interactions determine the overall dynamics of the interacting coupled system, and the role of these processes in the upper layers of the ocean must be understood before predictability is achieved with an acceptable degree of accuracy.

In the Atlantic, two modes of ocean-atmosphere interactions have been isolated as important in the genesis of climatically important sea surface temperature (SST) anomalies. One is an *El Niño*-like mode, which is mainly wind-driven; and another is a mode that involves subtropical-tropical interactions, explained as being mainly driven by a wind evaporation-SST positive feedback, generating the so-called Atlantic SST Dipole (see Servain *et al.* 1998 and references therein). This *dipole paradigm* has been challenged by a number of authors both by use of more advanced methods of analysis of the SST datasets (Mehta, 1998), or by analysis of subsurface data (Vauclair and du Penhoat, 2001), where it is shown that the dipole is not confirmed by data analysis. Despite these results of data analysis, many simple models suggest that a surface dipole mode may be a process driven by the wind evaporation-SST positive feedback mechanism (Chang *et al.* 1997; Xie, 1999), where the negative feedback necessary to quench an unbounded growth of SST anomalies is accomplished by ocean currents, but in an unspecified manner.

The main periods of variability of this surface *dipole mode* are found in the 12-13 year and in the quasi-biennial bands (Servain, 1991), with its north side having a certain lag relative to the south. Mehta (1998) shows that the decadal band occurs preferentially in the southern hemisphere side of the dipole, and with different main period in the north.

Among some of the open questions of interest, we may list the following:

1. What are the circulation processes through which the Atlantic Ocean can accomplish the negative feedback needed to stabilize unstable oscillations in the interhemispheric SST gradients appearing in the simple models ?
2. What is the role of the Subtropical-Tropical Cell (STC) (Liu and Philander, 1994; McCreary and Lu, 1994), if any, in relation to these oscillations?
3. If the STC plays a role, how does the southern STC interact with its northern counterpart, and what are the transport pathways closing an inter-hemispheric shallow exchange cell?
4. Can the circulation and transport variability in the lower branch of the Atlantic STC be studied by altimeter-derived flow field estimates based on sea surface height fields?

We dedicate this article to provide preliminary answers to question 4 and some issues related to question 3. The STC processes involve basically an off-equatorial mixed layer poleward Ekman flow, and equatorward geostrophic flows just below the mixed layer, but still in the upper 200 m. The Equator and the eastern ocean are characterized by the vertical advection of subsurface water feeding this circulation cell. The western subtropics is the main region where the mixed layer detains water to feed the geostrophic flow.

In the Atlantic, the upper layer flow does not present symmetry between the two hemispheres. In this ocean, the cross-equatorial southeasterly wind field and the slanted Brazilian northeast coast causes a northwestward net transport by the Ekman currents, and a geostrophic flow, below which may be in the same direction north of 5°S. This suggests that the simplest ocean STC models with rectangular basins may have limited applicability in the Atlantic. While the surface wind stress and Ekman flow fields and transports in the mixed layer may be estimated by use of scatterometer wind measurements, the determination of the upper thermocline current fields just below the mixed layer by satellite altimetry, with the same simplicity, is a matter of current research.

The expensive methods of altimeter data assimilation into ocean models have been under study for some time, and have also been applied in a monitoring mode by leading laboratories (see, e.g., Malanotte-Rizzoli, 1996). However, we should point out that very few studies

involving validation of current estimates obtained from these models have been presented in the published literature. The lack of moored measurements of the subsurface salinity field based on sensor data of acceptable quality is one of the present-day problems faced by these models (Segschneider *et al.*, 2000), with a direct impact on the accuracy in the currents obtained. Two illustrative examples of investigations related to the STC with realistic model basin geometry are the model works by Malanotte-Rizzoli *et al.* (2000) and Lazar *et al.* (2002), concentrating on the study of the seasonal cycle of the STC transfer of subtropical thermocline waters into the Equatorial Undercurrent (EUC). The results of these studies suggest that horizontal transfers in the lower layer just above the thermocline level are made through complex exchange windows, which are influenced by the equatorial upper ocean zonal current distributions. The exchange window in the North Atlantic involves a large longitude interval (open ocean), where it is believed that the equatorward pathway is mostly a zigzag flow due to the strong zonal currents. The South Atlantic model work indicates that the only important exchange window is the western boundary. However, there is a open-ocean convergence of southern waters in the lower branch of the STC into the EUC through a northward veering branch of the North Brazil Current (NBC) flow at 3°S, seen in Lazar *et al.* (2002).

In order address questions 3 and 4 stated above, we are faced with the traditional difficulty of the singularity of the geostrophic balance equation over the Equator. We had been investigating how to extend the above-mentioned equation into the Equator, and we found two possible formulations that solve this problem based on the shallow water equations on the beta plane. The simplest formulation is described in the present work.

This work is organized as follows. Section 2 contains the derivation of the equation for the zonal velocity component valid at all latitudes, and still based only on slopes and curvatures of the sea surface height. Section 3 and 4 present the data sets used and the data processing methods, respectively. Section 5 shows the comparisons of the altimeter-derived fields against *in situ* measurements. Section 6 describes the mean, the annual cycle and interannual variability of the altimeter-derived circulation fields, and contrasts our results with those obtained from model studies made by other authors. Section 7 presents transport patterns, open ocean windows for interhemispheric transports and interannual variability of total meridional transport. Section 8 discusses the main conclusions of this work. Appendix describes the time filter used to obtain the separation of the zonal and meridional current velocity and transport data sets into annual and interannual period bands. This method was preferred to the more traditional one based on multi-annual averages for each month because it makes feasible an easier account of all of the variances involved. This method also makes possible to keep track of the small phase and amplitude interannual *vacillations* in the annual cycle during the study period.

2. ESTIMATES OF CURRENT VELOCITY FROM SSH SLOPES AND CURVATURES

It is well-known that the lowest-order upper layer time-dependent (time scale larger than a few days) ocean dynamics can be accounted for by the Ekman and the geostrophic balances, which can be obtained independently from wind stress and surface height data (e.g. Gill, 1982). The problem with the geostrophic approximation is its traditional singularity on the Equator. However, several linear and nonlinear theories of both steady- state and time-dependent equatorial circulation indicate that the EUC is in geostrophic balance, although the standard f-plane geostrophic formula is not applicable at the Equator. The use of the meridionally differentiated form of the geostrophic equation has been studied by several authors to estimate the time-varying EUC flow in the Pacific Ocean, together with the standard form

for the off-equator zonal currents (Picaut *et al.*, 1989; Picaut *et al.*, 1990; Picaut and Tournier, 1991). The so-called equatorial geostrophy approximation for zonal flows is based on meridional second derivatives of SSH, obtained by a Taylor expansion near the Equator, assuming that the sea surface slope is negligible there, and can be discarded as noise. Many authors (see Lagerloef *et al.*, 1999, and references therein) have suggested methods to fit the off equatorial with the equatorial geostrophy equation.

We present here a alternative methodology to extend the geostrophic approximation into the Equator. The working hypothesis is that the zonal scale of order greater than 600 km is much larger than the meridional scale of 300 km for the EUC, the zonal current being of order of 1 m/s, and the upper layer thickness in dynamic balance being of the order 100 m.

We start with the shallow water equations for a single baroclinic mode, which may be written down in terms of the sea surface height variable, and assume that the flow is divergence-free:

$$(f + \zeta)\hat{\mathbf{z}} \times \mathbf{v} = -\nabla B, \quad (1a)$$

$$\nabla \cdot \mathbf{v} = 0. \quad (1b)$$

Here, $B = g\eta + (1/2)(u^2 + v^2)$, $\zeta = \hat{\mathbf{z}} \cdot \nabla \times \mathbf{v}$, and $\mathbf{v} = u\hat{\mathbf{x}} + v\hat{\mathbf{y}}$, where u and v are the horizontal velocity components in the eastward and northward direction respectively, g is the acceleration of gravity, and η the instantaneous sea surface height relative to the geoid, not to be confused with the altimeter-derived sea surface height anomaly, $\hat{\mathbf{x}}, \hat{\mathbf{y}}, \hat{\mathbf{z}}$ are eastward, northward and upward unit vectors and f is the Coriolis parameter. Taking the divergence of (1a):

$$\beta u + \hat{\mathbf{z}} \times \mathbf{v} \cdot \nabla \zeta - (f + \zeta)\zeta = -\nabla^2 B, \text{ where } \beta \text{ is the meridional derivative of } f, \text{ and} \quad (2)$$

expanding (2) in terms of the expressions for B and ζ :

$$f\zeta = [\beta + (\nabla \cdot \mathbf{v})_x]u + \nabla^2(g\eta) + u_x^2 + v_y^2 + 2v_x u_y + v(\nabla \cdot \mathbf{v})_y, \quad (3)$$

where the x and y subscripts denote derivatives. Taking ζ from the meridional component of (1a):

$$f + \zeta = -(1/u)(g\eta_y + uu_y + vv_y), \quad (4)$$

and inserting (4) in (3), we obtain:

$$au + b + (c/u) = 0, \quad (5a)$$

$$a = \beta + (\nabla \cdot \mathbf{v})_x,$$

$$b = g\nabla^2\eta + f^2 + u_x^2 + v_y^2 + v_x u_y + u_x v_y + v(\nabla \cdot \mathbf{v})_y, \text{ and}$$

$$c = gf\eta_y + g(\eta_x v_y - \eta_y u_y). \quad (5b)$$

Using (1b) we can express the exact result in (5a) and (5b) with the coefficients:

$$a = \beta,$$

$$b = g\nabla^2\eta + f^2 + u_x^2 + v_x u_y,$$

$$c = gf\eta_y - g\nabla\eta \cdot \nabla u. \quad (5c)$$

Equation (5a) is a quadratic equation for u , and coefficients in (5c) are exact for flows with zero divergence. A simple scale analysis shows that in most situations the terms in u - and

v- derivatives may be neglected. To this end, we must first use the hypothesis that the sea surface height field changes, reflect the pycnocline depth changes:

$$g\eta \approx g'h,$$

where g' is the reduced gravity, η is the upward measuring sea surface height, and h is the corresponding downward pycnocline depth changes (see Gill, 1982 p.119). The mean depth of the pycnocline has a scale $H = 100$ m. If we assume that the Kelvin wave speed has a scale of $c = 2$ m/s, then $c^2 = g'H = 4$; and we may use the distance scales for x as $L = 600$ km, for y as $l = 300$ km and the zonal current speed u as $U = 1$ m/s. The scale for v is derived from (1b), which is then $V = (l/L)U$. We can then obtain the normalized values for (5a) and (5c), so that the coefficients in (5c) become:

$$\begin{aligned} a &= R_0, \\ b &= B_u(h_{yy} + \epsilon_L^2 h_{xx}) + y^2 + R_0^2 \epsilon_L^2 (u_x^2 + v_x u_y), \\ c &= \left(\frac{B_u}{R_0}\right)[(y - R_0 u_y)h_y - R_0 \epsilon_L^2 h_x u_x], \end{aligned}$$

where $R_0 = U/\beta l^2$ is the equatorial Rossby number, $\epsilon_L = l/L$, and $B_u = g'H/(\beta l^2)^2$ is an equatorial Burger number. It can be seen that $B_u \approx 1.3$ while $R_0 < 1$, which justifies our approximation below, where the u-and v-derivatives and the second x-derivative of u are neglected. We made a thorough study of both roots of the quadratic equation, and concluded that only one of the roots was valid, being:

$$u = \left(\frac{1}{2\beta}\right)(-b + \sqrt{b^2 - 4\beta c}), \quad (6a)$$

$$b = g\eta_{yy} + f^2,$$

$$c = gf\eta_y. \quad (6b)$$

We may justify the use of (6b) even on the Equator ($c = 0$). There, the non-dimensional discriminant $b^2 - 4ac = B_u^2 h_{yy}^2 - 4B_u R_0 u_y h_y$. This means that second term on the right hand side is negligible in relation to the first term. Off the Equator, this expression is more general than the geostrophic balance equation for zonal flows, since if $b = f^2$ and $b^2 \gg 4c$, then $u \approx -c/\beta b = -g\eta_y/f$, a result obtained by Taylor expanding (6a).

Equation (6a) incorporates some cyclostrophic effects as well. We found that in the vicinity of strong eddies the pressure gradient represented in c is such that the term in the square root may become negative, a situation which we avoided by using only the real root at these grid points. We speculate that in nature such pressure gradients never become larger, and this situation must occur only due to imperfect mapping. We also found that the solution along the Equator is continuous with the off-equator circulation field:

$$u = \frac{1}{2\beta}(-b + |b|), \quad (7)$$

which does not allow a westward current over the Equator. When the current over the Equator tends to zero, we found that the v-field becomes dominant, corresponding to a veering or divergence of the flow. This one-sidedness in (7) is also consistent with the observation that westward flows due to the northern branch of the SEC are always confined to the mixed layer, extending to greater depths only off the Equator (Gill, 1982). This is interpreted as confirming

that the SEC over the Equator is better described as a remnant of the Yoshida jet, which is not a geostrophic current, but an Ekman current. A very good description of this subject may be found in chapter 4 of the book by Philander (1990). The finite-difference implementation of (6) is described in the next Section.

To calculate the meridional velocity field, we might integrate (1b) using (5) for the u -field. However, we did not find a proper analytical closed form solution without singularities as we did for the zonal current. Moreover, numerical integration also presented problems with the geometry of the western boundary. Therefore, we decided to use the geostrophic approximation instead. Since v is usually small (less than 50 cm/s) near the Equator, we first tested the applicability of a simple regularization of the type $1/f \rightarrow f/(f^2 + \epsilon^2)$ to compute v from the geostrophic formula, avoiding the calculation of higher (meridional-zonal) derivatives. However, an examination of Ship-mounted Acoustic Doppler Current Profiler (SADCP) data indicates that v is not zero at the Equator. Therefore, an assumption of $v = 0$ at the Equator is not realistic. Our conclusion is that v is geostrophic very near the Equator and its value can be well estimated from a spline interpolation scheme to complete the geostrophic v -data near the equator (between 1°N and 1°S).

3. DATA

3.1. Altimeter data

We used the collinear sea surface height anomalies (SSHA) from Topex/Poseidon (T/P) and ERS2 satellites distributed by the NASA Ocean Altimeter Pathfinder Project. Data from each satellite had been processed by the Pathfinder team, with the standard altimetric corrections, including the inverted barometer, interpolation into reference ground-tracks at 1 s sampling (approximately 7 km), and referenced to the mean sea surface GSFC98 (Wang, 2000). A more detailed description on this issue can be found in Koblinsky *et al.* (1999). Since the ERS2 data set is shorter than the T/P (T/P begins in 1992 while ERS2 in 1995), we only used data with common time that spans from 13 May 1995 to 20 November 2000. Therefore, our T/P collinear data set consists of 205 repeat cycles (one T/P cycle has about 10 days) and the ERS2 of 58 cycles (one ERS2 cycle has 35 days).

3.2. *In situ* data

To validate our estimates, we used the *in situ* data from western moorings of the PIRATA Program (Servain *et al.*, 1998), and from Etambot 1 and 2 cross-equatorial cruises of World Ocean Circulation Experiment (WOCE) (Diggs *et al.*, 2000; WOCE, 2000) (Figure 1). The PIRATA data consists of the daily time series of dynamic height relative to 500 m from 4 moorings located at 0°N-35°W, 4°N-38°W, 8°N-38°W and 12°N-38°W. These moorings started to collect data in 1998, except for the last one that started in 1999. For the computation of dynamic height, the PIRATA program uses the temperature and salinity measurements taken *in situ* and the standard temperature-salinity (T-S) relationship from the Levitus climatology of 1994. This T-S relationship is used to complete the gaps in salinity data, since the temperature is taken at 11 depth levels (from surface to 180m at depth intervals of 20m, and at 300m and at 500m) and the salinity is taken at only 4 depth levels (1m, 20m, 40m and 120m). The Etambot 1 and 2 cruises are part of the WOCE repetition line, and were performed in September 1995 and April 1996, respectively. During these cruises conductivity-temperature-depth (CTD) and SADCP data were collected, and these were analyzed by Arnault *et al.* (1999) and Bourlés *et al.* (1999). In these works, a partial retroflexion of the NBC south of the Equator was observed, consistent with observed eastward jets above the EUC. From all the cruise legs we only used those shown in Figure 1, since the rest were taken very close to the 1000 m

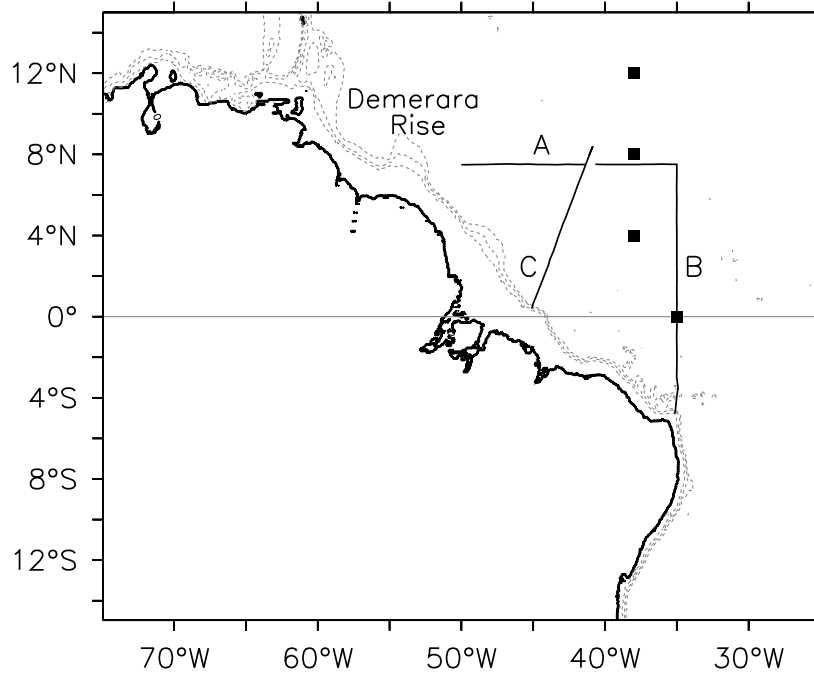


Figure 1. Section map of the study area including the WOCE-Etambot cruise legs, which obtained the hydrographic and SADCP data used in this work, and the four PIRATA mooring sites (squares). Track A is along 7.5°N and B along 35°W . 200, 1000 and 2000 bathmetric contours superimposed.

isobath, the cutoff depth of our gridded data.

4. DATA PROCESSING

4.1. Circulation fields from SSH data

The first step in the data processing consisted in the mapping of the SSHA collinear data into a $0.25^{\circ} \times 0.25^{\circ}$ regular grid (approximately $27 \text{ km} \times 27 \text{ km}$) covering the tropical Atlantic between 15°N - 30°S . A smaller area bounded by 15°S - 15°N and 70°W - 25°W , with 205 cycles of 10-day time steps, was selected for the present work. For both collinear data sets the outliers were first eliminated and the gaps interpolated along track using a cubic spline (Halpern *et al.*, 2000). The ERS2 data were adjusted with T/P data using the offsets between missions (see Koblinsky *et al.*, 1999). Note that the Pathfinder ERS2 data had already been corrected for an estimated instrument bias of 40.9 cm.

The mapping operation was performed using an objective analysis technique following the procedure of Kessler and McCreary (1993). The values of mapping parameters were chosen to retain the meso and the large-scale features typical of the region, which proved to be coherent with measured *in situ* data from moorings of the PIRATA Program.

The second step was to estimate the actual sea surface height. To accomplish this, we sum the time-varying anomalies with a mean (long-term multi-year average) dynamic height field, obtained from hydrographic data. We use the high resolution ($0.25^{\circ} \times 0.25^{\circ}$) Boyer-Levitus

climatology (BL) (Boyer and Levitus, 1997) to obtain a dynamic height referenced to 1000 m. The choice of BL and the depth reference is dictated by a compromise made between a small reference velocity at depth, and the desired proximity to the western boundary. The usual reference depth at equatorial areas to establish the level of no motion has been 500 m. However, 1000 m can be also acceptable, in view of the measurements recently made at this depth by Molinari *et al.* (1999), which suggest an average velocity of 10 cm/s at this depth. The SSH data is filtered using a special spatial multi-channel singular spectrum (MSSA) filter (Plaut and Vautard, 1994) to eliminate short wavelength noise but keeping mesoscale features. This filter consists of decomposing each derivative-data field in reconstructed components (RC's), and determining the most energetic spectral peak in each of them. The filtered fields are obtained by superposition of the RC's with maximum spectral peaks corresponding to wavelengths larger than 300 Km. In this way, there was no attenuation or spreading of true naturally occurring spatial peaks, but the noise was eliminated.

From the filtered SSH maps the circulation fields are derived using the methodology described in section 2. The computations of the first and second derivatives is done using finite-differences and the same adaptive filtering cited above. The one-sided differences are used at the boundaries, while the centered-differences at interior points. The filtering after computation of each derivative was done to avoid losing boundary points, spreading and losing amplitude on true mesoscale features.

4.2. Computation of transport fields

The transport pathways are estimated in a simple manner by mapping them in units of distance perpendicular to the transport direction. The meridional transport in units of zonal distance ($T_y(x)$) and zonal transport in units of meridional distance ($T_x(y)$) is an easy means of exhibiting the non-integrated transports across latitude circles and meridians, respectively.

In a single baroclinic mode model, we first assume that the mean geostrophic layer has a thickness of $H = 100$ m, the lower motionless layer has a $\sigma_t = 26.5$, and the upper layer a $\sigma_t = 22.5$, therefore:

$$Ty(x) = (H + h(x, y))v(x, y), \quad (8a)$$

$$Tx(y) = (H + h(x, y))u(x, y). \quad (8b)$$

The integrated transports may be obtained by integrating the first expression in x between two longitudes, and the second expression in y , between two latitudes. Here, $h = (g/g') * \eta$ is the changing depth of the pycnocline as a function of the η .

4.3. Comparison of *in situ* data and altimeter-derived fields

The altimeter-derived fields described in the previous section, have been compared with *in situ* measurements:

a. SSHA time series with dynamic height obtained from PIRATA moorings. As suggested by Rebert *et al.* (1985), before performing the comparisons, the daily time series from PIRATA moorings were averaged into 10-day interval time grids. The time series of SSHA near each mooring were constructed by extracting the values of SSHA at grid points at the mooring positions (see table 1),

b. SSH with dynamic height derived from CTD casts obtained in the Etambot cruises, both referenced to 1000 m. In order to do so, the CTD track data were interpolated into a finer 0.25° grid, and

c. Circulation (zonal and meridional components) with measurements of SADCP and CTD-derived velocities from the Etambot cruises.

The following statistical parameters were computed from each comparison above: minimum, maximum, mean, standard deviation (*std*), signal-to-noise ratio (*snr*), correlation coefficient (*r*), the root-mean-square (*rms*), and *rms* difference values. The *snr* and *rms* terms used here follow the same definitions as those used by the Pathfinder team in their validation efforts (Koblinsky et al., 1999). Results from these comparisons are presented in Section 5.

4.4. Band-limited circulation and transport fields

A special adaptive filtering method was used to separate the circulation and transport fields into components in the period bands of interest:

1. Intra-seasonal: less than 150 days,
2. Semi-annual: between 150 and 240 days,
3. Annual: between 240 and 400 days,
4. Inter-annual: more than 400 days.

The filtering procedure is based on a combination of empirical orthogonal function (EOF) and MSSA methods for the time-dependent principal components. These methods allow to record not only the variance explained by each band-limited data set, but also the spectral peak periods and their energy within each band. Further descriptions of these methods can be found in Appendix B.

There is a strong motivation for using these methods, as opposed to using simple climatological averages and anomalies relative to the annual cycle. Analysis of T/P and tide gauge sea level data near Fortaleza (3°S; 39°W) showed interannual variability in period and amplitude of the annual cycle, with 1996-1997 exhibiting a period of 255 days, and the smallest amplitudes. These phase and amplitude changes in the annual cycle are preserved with such a filter, but do not have any signature if we use the more traditional methods of analysis. We believe that such a method of analysis can, in principle, be interesting for our future studies on prediction of ocean currents.

5. COMPARISON OF *IN SITU* DATA AND ALTIMETER-DERIVED FIELDS

5.1. SSHA time series and dynamic heights from PIRATA moorings

Table 1 summarizes the results obtained from regression analysis for each mooring, showing a good agreement between the SSHA and the surface dynamic height (ref. 500 m). All the results listed below are significant at the 95% level. The analysis showed that it is possible to obtain a single regression line for all the western moorings listed above. Therefore it is clear that the SSHA field reflects a first baroclinic mode quite well in the PIRATA sites in the northern hemisphere.

Table 1

Results of the regression of SSHA and dynamic height (500 m reference depth) from data from PIRATA moorings, where *r* is the correlation coefficients and *N* is the number of observations (10 day-cycles). Units of offset are in cm.

Mooring	<i>N</i>	offset	slope	<i>r</i>
0°N-35°W	86	91.52	0.71	0.83
4°N-38°W	39	93.96	0.96	0.92
8°N-38°W	82	81.81	0.78	0.69
12°N-38°W	37	79.20	0.92	0.88

Table 2

Altimeter-derived SSH (ALT) and CTD dynamic height comparisons for tracks A, B and C, including the *rms* (of differences), *r* (correlation coefficients). Units are in cm.

Track date	N	mnCTD	mnALT	mxCTD	mxALT	stdCTD	stdALT	<i>rms</i>	<i>r</i>
A 09/95	59	130.34	135.80	152.08	148.49	4.82	3.09	3.36	0.72
B 09/95	47	136.00	138.45	158.03	153.78	6.45	4.87	2.77	0.94
C 09/95	11	125.17	144.15	151.49	155.64	9.03	4.48	10.2	0.90
A 04/96	55	127.37	133.84	151.95	144.43	6.60	2.84	5.87	0.54
B 04/96	49	122.23	129.56	138.46	141.35	3.36	3.59	5.30	0.67
C 04/96	18	134.32	135.90	146.72	149.63	4.12	3.71	3.90	0.53

mn stands for minimum values and *mx* for maximum values. Sep 95 refers to Etambot 1 and April 96 to Etambot 2.

We notice that at the mooring located at 8°N the correlation is lower (0.69). We attribute this to the fact that the dynamic height calculation based on the salinity values obtained from the T-S relationship is faulty, especially because the lack of salinity data acquisition at the maximum salinity region at 80 m depth. The studies of Maes (1998) and Vossepoel *et al.* (1999) support this conclusion, and the former author also estimates the influence of the barotropic component as being negligible importance in relation to the baroclinic. This problem was further investigated by Segschneider *et al.* (2000), who described problems associated with the salinity influence on the dynamic height estimates in a broad region over the tropical north Atlantic in May 1999. They suggested that the salinity maximum would be at 120 m, when it really occurs at 80 m, with a probably strong annual variability. These salinity effects are now known to be important for the dynamic height estimates (Mayer *et al.*, this volume), and SSHA assimilation into operational ocean models (Maes, 1998). This problem can be corrected using of the data from a internally recording salinity sensor placed at that depth during the PIRATA II in cruise in 1999. The correlations are similar between SSHA and the depth of the 20°C isotherm (Z20) (between 0.61 and 0.86), but improve when the pycnocline depth is used in place of the Z20 (not shown).

5.2. SSH and dynamic height from the CTD Etambot cruises

Table 2 shows a statistical comparison between altimeter SSH and dynamic heights derived from Etambot cruises. The correlation coefficients (*r*) for Etambot 1 are larger as compared to those of Etambot 2. The plots (not shown) of the dynamic height and SSH data of Etambot 2 permit clear interpretations of these discrepancies. For track A the dynamic height has very high amplitude spikes, one near 40°W (change of 20 dyn cm in 2° of longitude), while the SSH data do not capture this type of feature. We may note in Table 2 that the standard deviation of the CTD data is 2.5 times the standard deviation of the SSH data. Therefore it, is difficult to evaluate if this problem arises from inaccuracies in the CTD measuring system, or due to the SSH data. For track B SSH is larger than the dynamic height between 4-8°N by an average of 8 cm, while it is less than 4 cm elsewhere in the track. For track C both SSH and dynamic height show spikes along the track which differ in position by 50 km.

5.3. Current velocities and measurements of SADC and CTD-derived velocities

We here show results of the study to validate our methodology of computation of geostrophic currents based on dynamic heights and altimeter derived SSH. In relation to the SADC

Table 3

Correlation coefficients of CTD-derived velocity components with SADCP data at various depths for tracks A and B: (a) Etambot 1 (Sep 1995) and (b) Etambot 2 (April 1996)

(a)												
$depth(m)$	20	30	40	50	60	70	80	90	100	110	120	130
A v	0.50	0.46	0.37	0.33	0.25	0.19	0.16	0.12	0.11	0.07	0.04	0.13
B u	0.56	0.55	0.57	0.61	0.68	0.76	0.79	0.77	0.74	0.71	0.64	0.63

(b)												
$depth(m)$	24	32	40	48	56	64	72	80	88	96	104	112
A v	0.65	0.66	0.67	0.69	0.70	0.69	0.68	0.67	0.62	0.58	0.59	0.60
B u	0.81	0.83	0.82	0.79	0.73	0.73	0.77	0.78	0.77	0.75	0.72	0.69

u is zonal velocity and v is the meridional velocity.

vertical profiles used for this validation, the lateral resolution during the Etambot 1 cruise was around 1 km, while during the Etambot 2 the resolution was about 50 km due to difficulties with the SADCP data acquisition (Bourlés *et al.*, 1999).

Table 3 shows the correlations between the SADCP depth profiles and CTD-derived velocities over the ship tracks A and B. The meridional velocity, v , for track A in Etambot 1 (Table 3(a)) has the highest correlations near the surface, while the zonal velocity, u , along track B has the highest correlations between 70 m - 90 m. Table 3(b) shows the results of the Etambot 2, which present higher correlations. In this case, there is no significant depth dependence in the correlations between the surface and 100 m depth.

Table 4(a) shows the corresponding results of SADCP depth profiles with altimeter-derived velocities in Etambot 1. We see that the best correlations obtained for track A were at the 50 m - 70 m depth ranges for the zonal velocities. However, the correlations are maximum at the surface for the meridional component. Track B shows maximum correlations better defined at 70 m - 80 m. Table 4(b) shows the same results for the Etambot 2. The correlations are generally approximately 0.8, except to v in track B, and are better at subsurface depths, although these are not significantly different from the surface values. In the case of the track B, since during this time (April) the zonal wind is weaker and the EUC shallower, we speculate that the correlations are expected to be the same throughout the whole upper layer.

Figure 2 exhibits a comparison between the altimeter-derived zonal and meridional velocities over the Etambot 1 track B calculated from our methodology and the SADCP data for the depth of maximum correlation at 70 m. We also include the standard geostrophic estimate with the equatorial singularity for the zonal current, calculated from the same SSH data. Note the convergence between ours and the standard geostrophic estimates one degree away from the Equator in Figure 2a. The eastward flow is quite broad in the southern hemisphere, and seems to be centered at 1°S. This is consistent with the high resolution circulation model results of Schott and Boning (1991), which shows that the EUC core in August is not over the Equator, but to the south. Between 4°N-6°N the differences seem to be due to ageostrophic components (Garzoli and Molinari, 2001). For the meridional component the agreement is quite good between 2°S-6°N. Notice that at the Equator the meridional velocity is 20 cm/s to the south, suggesting a southward transport, which implies that the core of the EUC is not on the Equator and may be dominated by meandering, as seen in the annual cycle of Schott and Boning (1991).

Table 4

Correlations coefficients of altimeter-derived velocities with SADC data at various depths for tracks A and B: (a) Etambot 1 (Sep 1995) and (b) Etambot 2 (April 1996)

(a)												
$depth(m)$	20	30	40	50	60	70	80	90	100	110	120	130
A u	0.57	0.58	0.62	0.66	0.67	0.63	0.50	0.31	0.26	0.38	0.45	0.42
A v	0.82	0.77	0.69	0.63	0.58	0.53	0.46	0.35	0.26	0.20	0.14	0.15
B u	0.70	0.70	0.73	0.78	0.83	0.85	0.83	0.78	0.75	0.74	0.70	0.68
B v	0.51	0.47	0.49	0.58	0.68	0.75	0.77	0.76	0.74	0.67	0.57	0.52

(b)												
$depth(m)$	24	32	40	48	56	64	72	80	88	96	104	112
A u	0.79	0.79	0.79	0.79	0.79	0.79	0.80	0.81	0.80	0.82	0.83	0.80
A v	0.86	0.87	0.87	0.88	0.89	0.88	0.87	0.87	0.85	0.81	0.82	0.81
B u	0.88	0.86	0.82	0.80	0.79	0.83	0.87	0.89	0.89	0.87	0.84	0.82
B v	0.48	0.53	0.58	0.64	0.67	0.66	0.63	0.60	0.59	0.57	0.55	0.51

u is the zonal velocity and v is the meridional velocity.

We did not include the other plots for the Etambot cruises for brevity. For track B of Etambot 2, the correlations shown on table 4(b) are reasonable from the surface to 130 m for u , but only regular (0.67) around 60 m for v . However, we should note that during Etambot 2 there was a failure in the SADC, and only lowered ADCP data at CTD stations were obtained. This lower resolution SADC transect is, therefore, not very good for comparing with altimeter-derived currents, although the correlations look reasonable. For track A, both geostrophic and our equation underestimate the zonal currents in location with strong eddy components. This result is well-known (e.g. Arnault *et al.*, 1999) for synoptic data, but is probably averaged out when low-frequency flow patterns are considered.

The results presented in this section reinforce the idea that the SSH-derived currents reflect flows in the upper thermocline level, and the fact that the EUC core may be quite off the Equator in the western Atlantic. However, a possible limitation to the present method should be mentioned. There are transition regions where the compensation steric and dynamic subsurface effects may produce negligible surface expressions. In these regions, the correlation between SSH and the vertical density profiles are different from the simple single baroclinic mode approximation used here to estimate the geostrophic currents. As a consequence, the geostrophic current obtained from surface dynamic topography may be severely underestimated in these regions. This may be one reason why a zonally discontinuous core of the EUC is recorded in the sections which follow, instead of a continuous one.

6. ANALYSIS OF THE CIRCULATION FIELDS

As a result of the analysis of the partition of the data sets related to the zonal velocity (u) and the meridional velocity (v) by period bands, we found the following variances of the total variance related to each of the separated bands:

1. Intra-seasonal plus turbulence noise: 51%(u) and 78% (v),
2. Semi-annual: 9% (u) and 4% (v),
3. Annual: 27%(u) and 11%(v), and
4. Interannual: 8% (u) and 5% (v).

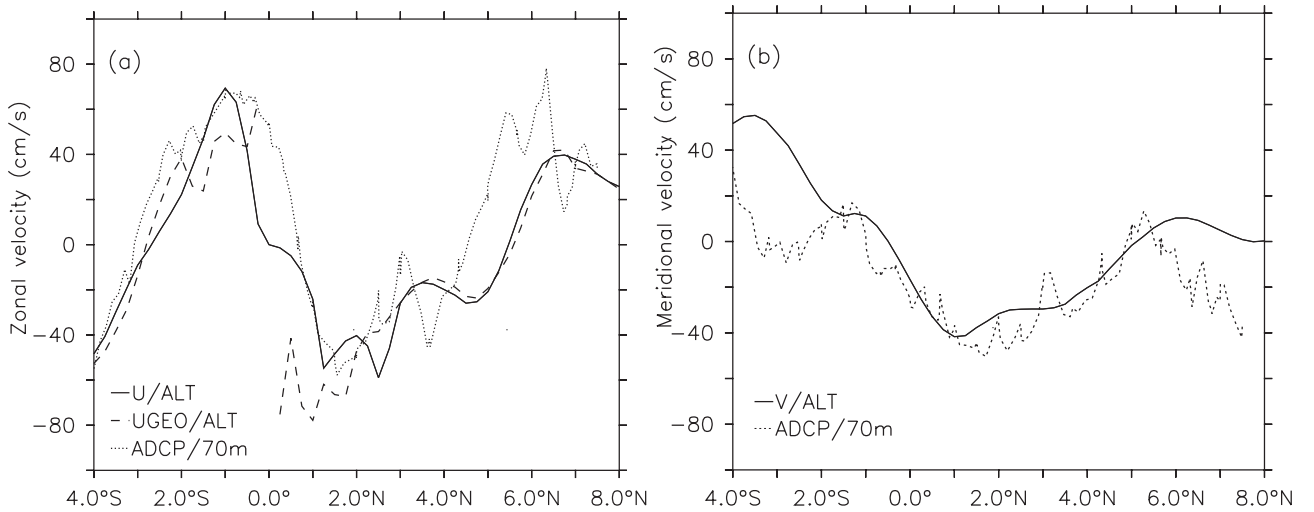


Figure 2. Comparing zonal and meridional velocities estimated with satellite derived SSH through use of equation (7), contrasted against the f-plane geostrophic estimate, and ADCP data at 70 m depth, Etambot 1 cruise (Sep 1995). Notice the good agreement of the meridional velocity estimate over the Equator, which is southward (20 cm/s).

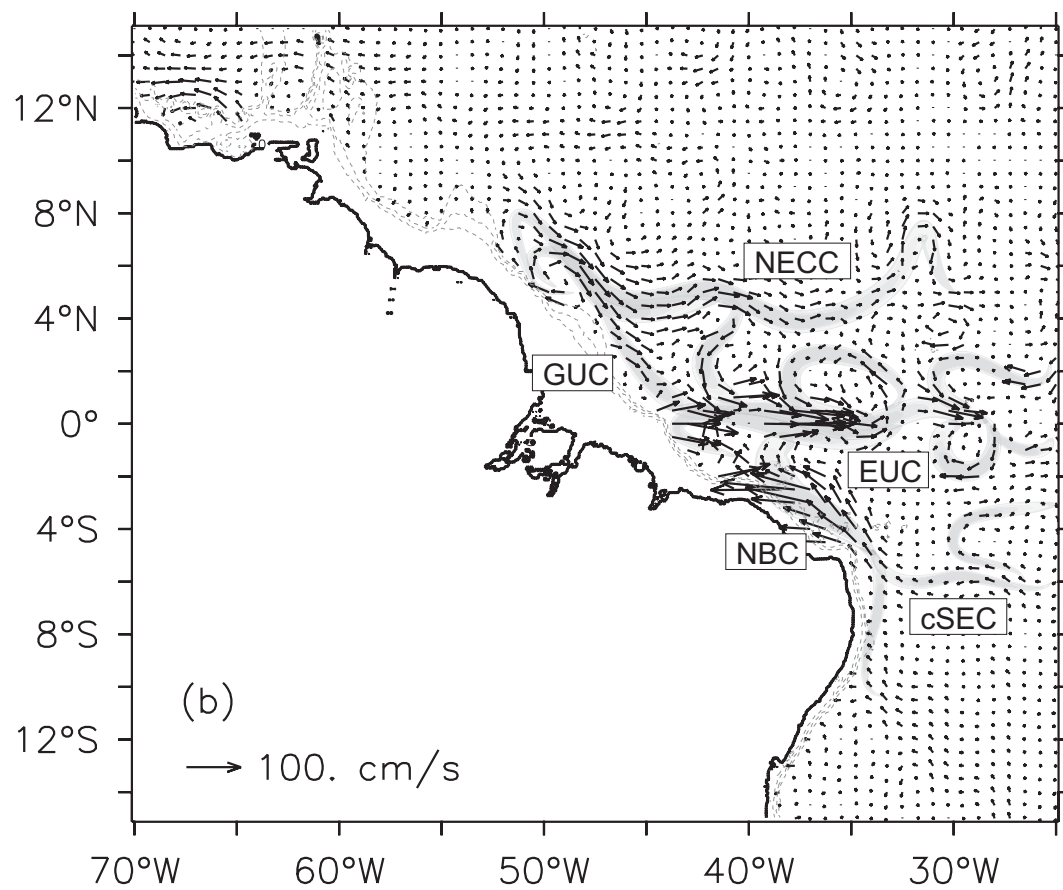
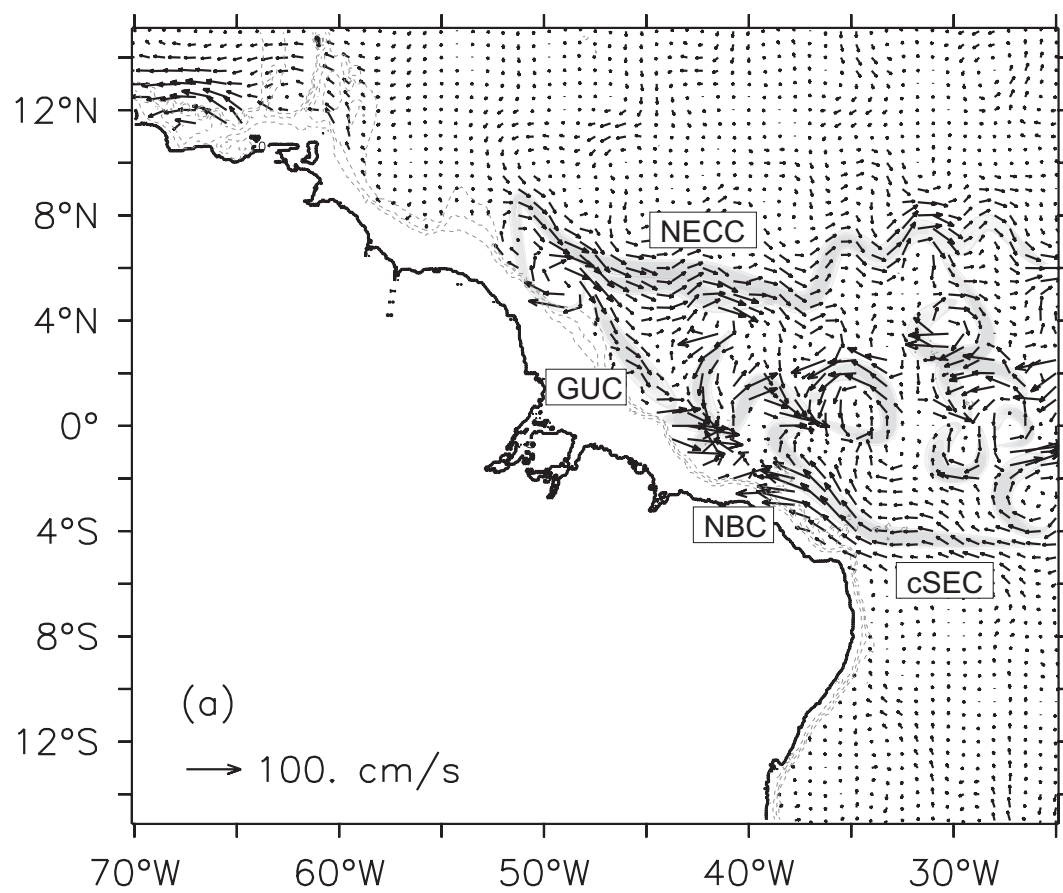
The first two bands cited above are not investigated in the present work. Spectral analysis within the interannual band, using autoregressive analysis, allow to estimate how the nonlinear trends in short time series may be best interpolated by a sum of sinusoids. This analysis shows that the nonlinear trends can be expressed as a sum of a quasi-biennial (QB) mode, and a 6.8 year period mode. Servain (1991) found that the tropical Atlantic SST interannual variability may be expressed as a sum of a QB and a 13 year mode. If we interpret the 6.8 year variability as possibly being a second harmonic of the 13 year component, the above results suggests that SST and geostrophic circulation modes may be related.

6.1. The mean currents

In this section three mean current fields obtained from three annual mean dynamic topography maps (reference depth of 1000 m), are described, as shown in Figure 3:

- a. The mean circulation based on sea surface dynamic topography obtained from the Boyer-Levitus 1997 climatology,
- b. The mean circulation based on the 100 m depth dynamic topography surface from the same climatology,
- c. The 5-year mean of the SSH-derived circulation time series, where the SSH grids are formed by adding the Boyer-Levitus sea surface dynamic topography to the altimeter-derived SSHA at each 10-day time step.

The mean surfaces shown in Figure 3 reveal mesoscale circulations that may be related to noise due to changing circulations, or may be related to true standing circulation modes. To discern between noise and mean modes in the true mesoscale, one should resort to altimetric observations (if these are standing oscillating features), *in situ* observing systems and eddy-resolving models. One interesting example of this type of situation may be found in the objective mapping of the mean SSH (relative to 750 m) of the South Pacific Ocean, presented by McCarthy *et al.* (2000). In their map, the warm-core East Cape Eddy off New Zealand is a typical example of a mesoscale feature in a climatological dynamic height map, which is not



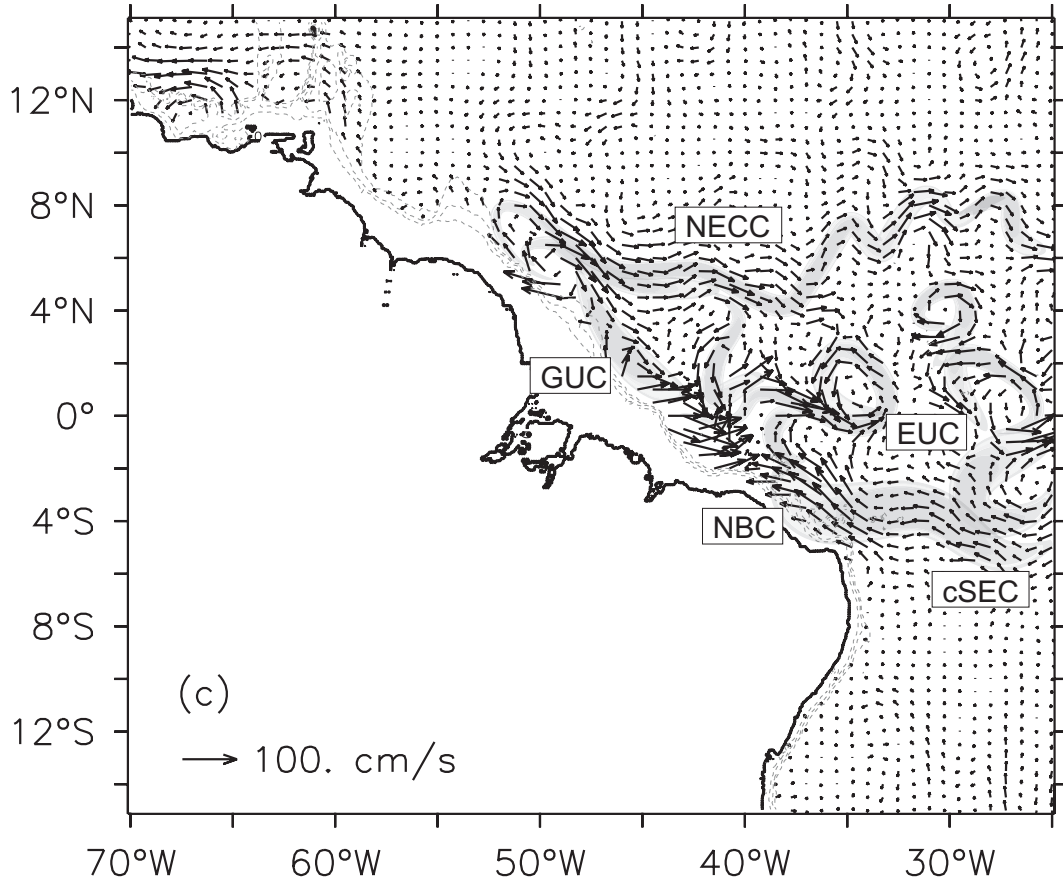


Figure 3. Mean circulation based on sea surface dynamic topography (a), 100 m (b) and 5-year average SSH data (c). See text for details.

noise at all.

Analysis of these three mean circulation fields does not show a continuous EUC signature between $1^{\circ}\text{N} \times 1^{\circ}\text{S}$. The EUC signature is zonally inhomogeneous, resulting from meridionally-aligned cyclonic eddy pairs north and south of the Equator, which causes only eastward currents at eddy current convergences. This is better seen in the Boyer-Levitus 100 m circulation field, where the eddy pairs and the EUC signature are connected (Figure 3b). These facts suggest that the EUC flow might be strongly connected to these mean cyclonic eddy pairs. However, the common view of the relation of the EUC with the subsurface dynamic height topography does not include stationary eddies.

The common view of the upper layer equatorial current system is based on the wind forced model described in Gill(1982), with a westward mixed layer current on top of a EUC during the early times after switching on the westward zonal wind. The EUC velocity may be related by equatorial geostrophy to the ridge in the dynamic height field which is formed below the mixed layer. A simple stratified model is described in more detail by Philander (1990). In particular, he shows that after the growth of the Yoshida jet is quenched by the arrival of the Kelvin wave, formed by reflection of the jet perturbation at the western meridional boundary. The jet itself is eroded very fast by meridional Ekman divergence. The EUC in this model is due to the second baroclinic mode current, which acts also to cancel the surface jet.

It should be noted here that reflection of baroclinic Rossby waves from a slanted model

western equatorial boundary has qualitative differences from the straight meridional boundary counterpart. The latter involves only Kelvin and boundary-trapped eastward propagating Rossby waves. In contrast, the slanted boundary reflection, in a model with vanishing lateral eddy viscosity, results in interference patterns of incident and reflected waves, which are not only Kelvin waves (Holvorcem and Vianna, 1992). It is shown in this latter work that meridionally propagating evanescent waves may not be of negligible importance, and may generate large amplitude standing wave patterns trapped near the Equator.

Away from the Equator, Figure 3c is in general consistent with the mean flow field at 133 m (Figure 1 in Schott and Boning, 1991). Between 10°N and the Equator, the flow is essentially eastwards at the open ocean, and to the southeast near the western boundary, attaining 50 cm/s near 5°N. Northwest of the (Demerara) continental rise at 8°N offshore Guyana, the flow is to the northwest. In Figure 1 of Schott and Boning (1991), it is important to note that there are also regions of maximum/minimum current intensity in the EUC pathway, which is reflected more dramatically in our Figure 3c.

The results of this section reinforce the conclusion that altimeter-derived circulation data relate more to the subsurface than to the surface structure in the western equatorial Atlantic. This fact has also been explicitly cited by many authors (e.g. Larnicol *et al.*, 2002). In the following sections we show the existence of trapped equatorial standing modes in the seasonal circulation, a fact that may explain why the wild mesoscale variability appears in the mean maps, including the maximum/minimum intensity patterns in the mean EUC signature, and the link to the standing cyclonic eddies which appear in the Figures above.

6.2. The seasonal cycle

The seasonal evolution is now illustrated using 10-day grids of the annual band data sets, for certain months of 1997 (February, April, July, September and November), in order to highlight major transitions in circulation patterns. We display pairs of figures representing anomaly and total flow fields, the latter being included to facilitate interpretations as compared to measurements.

We start the sequence of illustration with one corresponding to February 15 (10-20 Feb), 1997 (Figure 4a). Between 4°N-10°N, a band of westward anomaly flow is seen to be perturbed by a anticyclonic eddy confined between 40°W-50°W and 2°N-6°N, with intensity of approximately 25 cm/s. Figure 4b shows the influence of this perturbation in forming a cyclonic loop, with its southern limb being the remains of the North Equatorial Countercurrent (NECC) at 6°N, with intensity of approximately 40 cm/s, and with its upstream branch resembling the Guyana Undercurrent (GUC). The bifurcation at the Demerara Rise is present, with a northwest flow to the west and a southeast flow to the east. A meandering EUC appears between 2°N-2°S, with longitudinal variations in intensity. Between 1°S-4°S a meandering circulation is seen, representing the central branch of the South Equatorial Current (cSEC).

The circulation field appears to be more intensified in mid April (Figure 5). The anticyclonic eddy perturbation has its southern limb westward flow intensified (Figure 5a) while the NECC weakens considerably, but does not completely disappear (Figure 5b). The cSEC intensifies and converges into the EUC at 35°W. The EUC signature has an intensified structure between 1°N and the Equator (Figure 5b).

In mid July we notice that a sharp transition takes place in the anomaly field (Figure 6a). The anticyclonic eddy centered near 5°N-43°W observed in April (Figure 5a) changes into a cyclonic eddy. We now notice a broad retroflection signature between the Equator and 6°N, although we do not see the NBC pressed against the coast (Figure 6b). A double-core NECC can also be observed, with its northern branch around 8°N, and its southern branch around

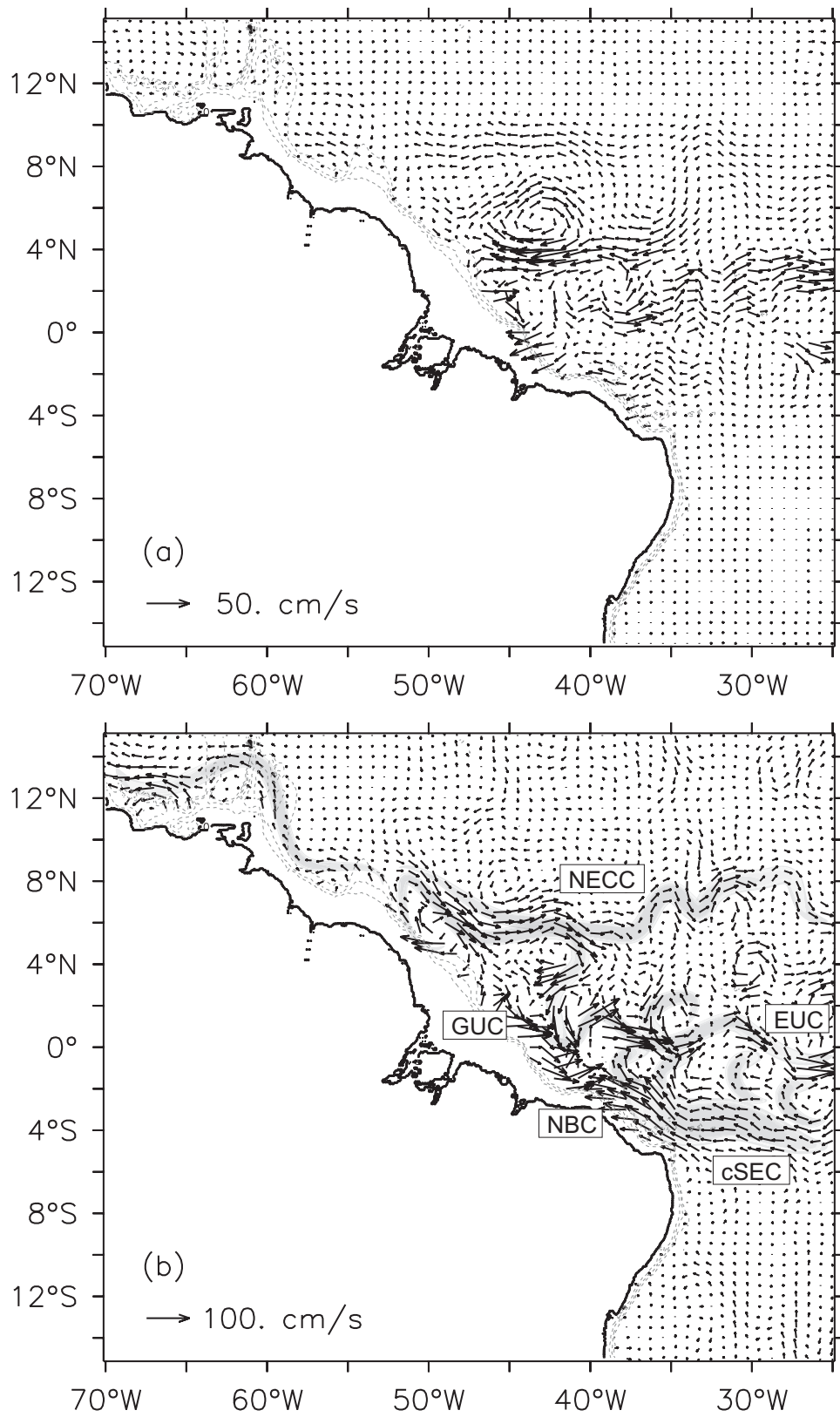


Figure 4. Mid February 10-day anomaly field (a) and 10-day anomaly plus the 1995-2000 mean (b) in the annual band data set. Signatures of the more intense currents (NECC, EUC, NBC, GUC, cSEC and nSEC) are indicated.

5°N. This double-cored NECC was first suggested in the model work by Schott and Boning (1991), and its existence is therefore confirmed here. These branches coalesce near 35°W. At 2°N, we notice the presence of a westward current resembling the northern branch of the SEC (nSEC). The EUC appears disrupted between 30°W-33°W, due to recirculations.

By mid September (Figure 7a), we notice a intensification of the current anomaly structures observed in July (Figure 6a), and the appearance of a strong large anticyclonic eddy pressed between 0°N-6°N. This feature forms a N-S pair with the cyclonic eddy, which appeared in July. The double-cored NECC is still seen, with the north core around 9°N, and a south core at 5°N, with a coalescence at 32°W at 8°N (Figure 7b). The strong south core of the NECC is mostly originated by the NBC retroflection at 8°N, near the Demerara Rise. A westward nSEC is also seen meandering around 2°N. The EUC, at this time (Figure 7b) has been quite disrupted by the cyclonic eddies. This is consistent with the Etambot SADC measurements taken in 1995 at 35°W, which showed an eastward velocity core at 1°S, and a southward subsurface velocity of 20 cm/s at the Equator. Moreover, the flow field in September 19, 1995, resembles the one in Figure 7b between 4°N-4°S (not shown here). These results suggest that the circulation near the Equator at 35°W is dominated by a annually recurring eddy, possibly due to equatorial wave dynamics.

In mid November, another transition phase seems to be setting in, with a broadening and intensification of the anticyclonic and a shrinking of the cyclonic eddies (Figure 8a). The meandering seen in the NECC core region at 5°N-6°N can be identified as being due to a wave (Figure 8b). The annual cycle of this meandering can be better observed in the time-longitude diagram of the meridional velocity perturbation (Figure 9). The disturbances propagate westwards from 32°W with a phase speed around 1.8 km/day. To the east, only a weak signature of a standing wave is seen. There are three crests in this wave pattern, a picture which is also consistent with the results presented by Schott and Boning (1991) (their Figure 2b). We suggest that this could be due to a Rossby wave interference pattern of the type described in Holvorcem and Vianna (1992) for intra-seasonal waves, although a more detailed model study must be carried out to obtain more definitive conclusions. No clear EUC signature is seen, although the zonal component between 0°N-1°S is eastward almost everywhere over the Equator. It appears that the EUC is disrupted by eddies. The origin of these eddies may be related to instability waves, or to waves driven by weather events, together with wave scattering from the western boundary. One example of the latter wave process in the TOGA-COARE area with a very high resolution model is presented by Dourado and Carniaux (2001).

6.3. Standing trapped annual equatorial waves and meandering

We have shown that during February to April the EUC signature is present, but dominated by meandering and longitudinal variations in the intensity. During the rest of the months, the EUC is disrupted, and the equatorial eastward flow is dominated by a sequence of counterclockwise eddies. Time-longitude diagrams of the meridional velocity at 0°N-2°N (not shown here) suggest a picture of a tightly standing wave mode throughout the year. The meridional velocity anomaly map for the annual cycle in mid January 1997 (Figure 10) exhibit two clear wave signatures: one consisting of three crests at 5°N, which are related to the NECC meandering, and another at 2°N and 2°S, with smaller wavelength. We believe that the latter might explain some of the high amplitude mesoscale features observed in the Boyer-Levitus climatology near the Equator, the observed EUC meandering, and the open-ocean windows for interhemispheric transport described in the following section.

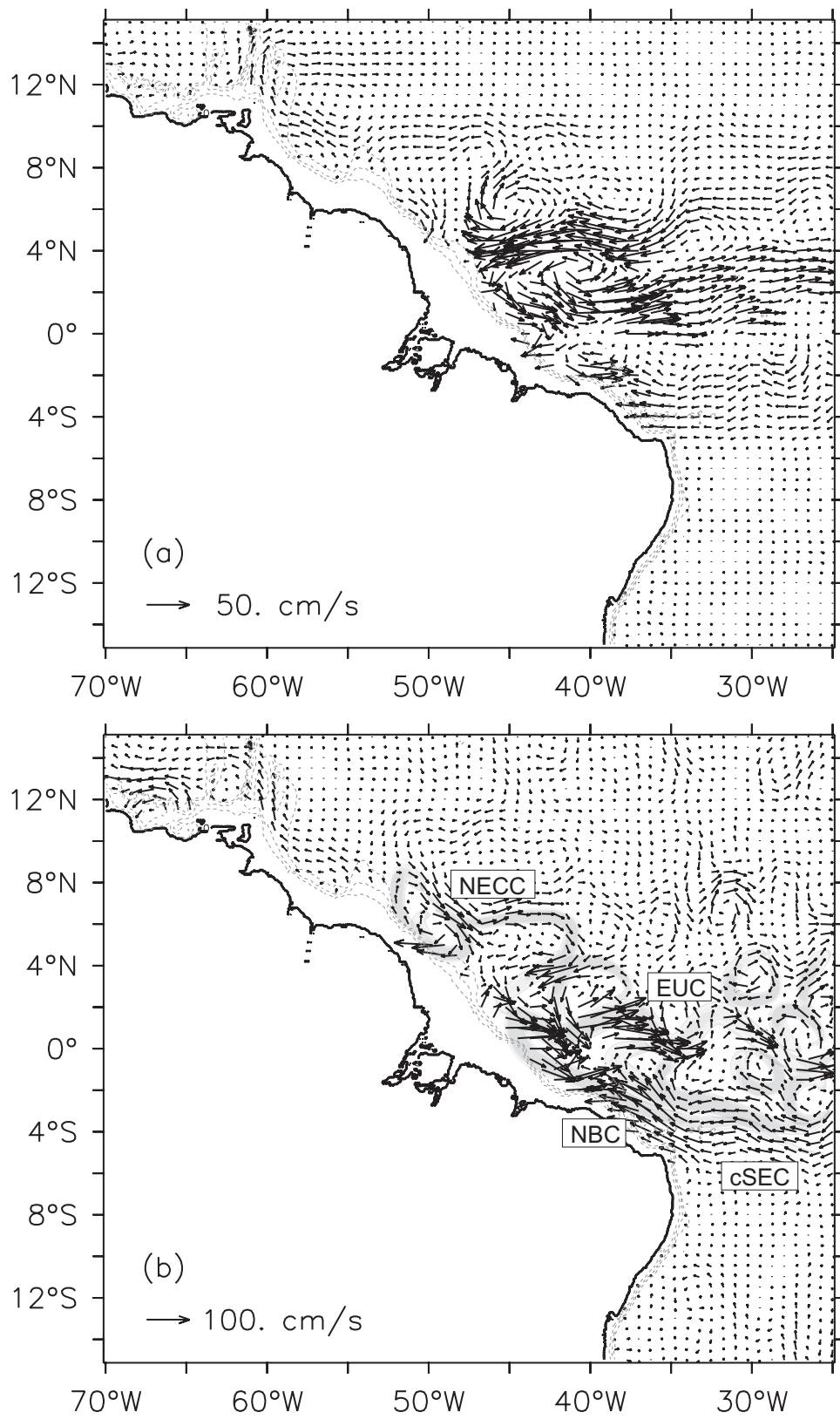


Figure 5. Same as Figure 4, but for mid April 1997.

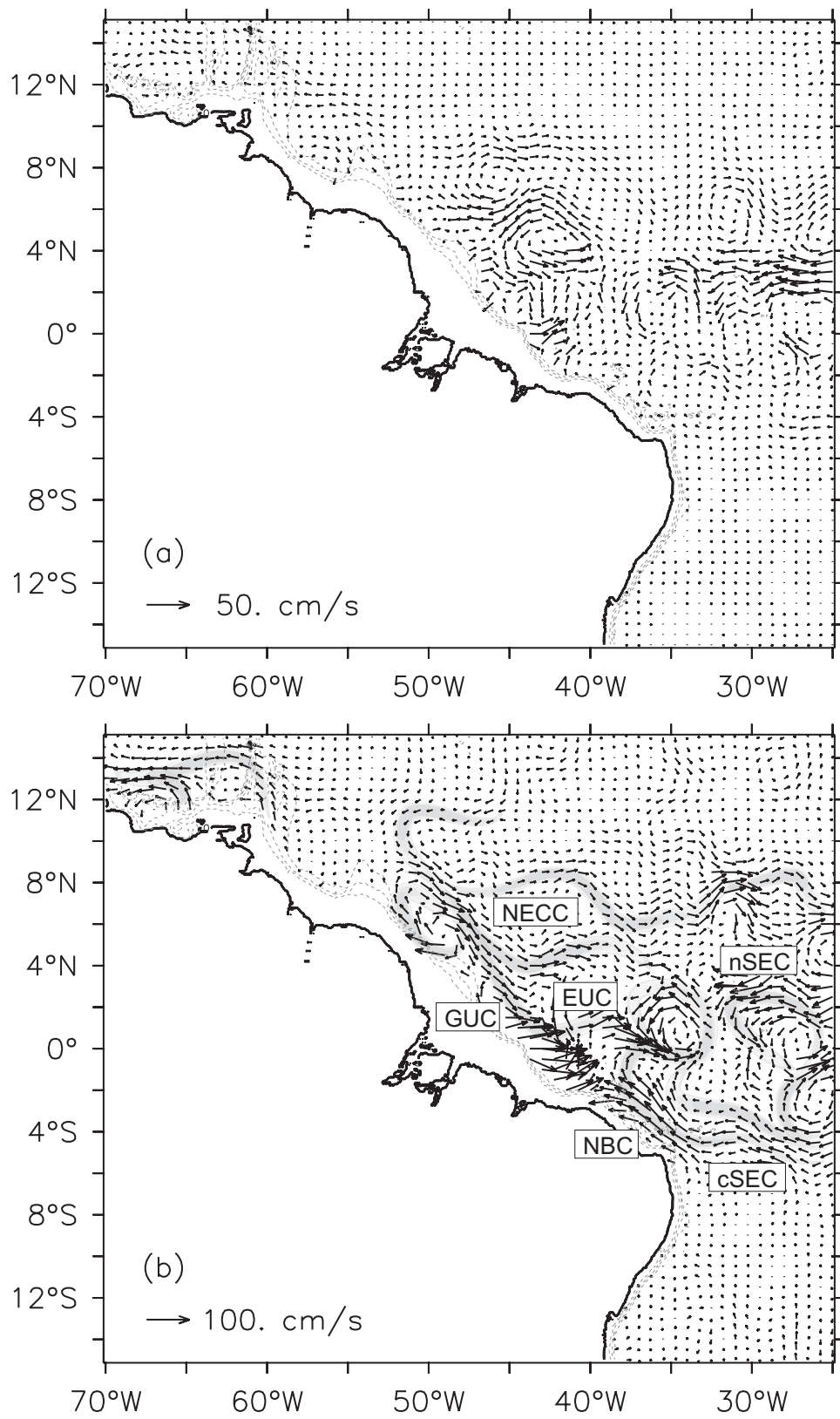


Figure 6. Same as Figure 4, but for mid July 1997.

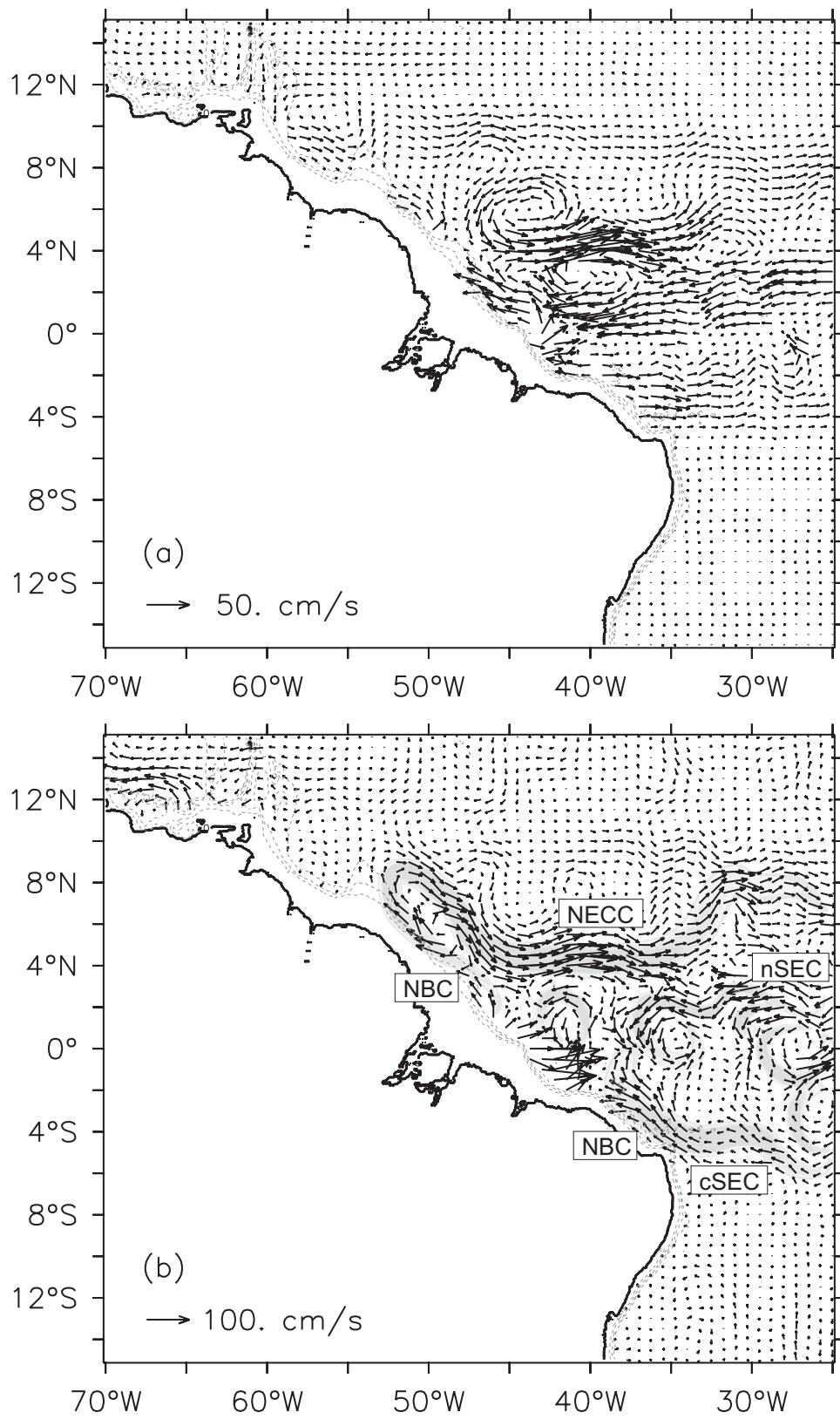


Figure 7. Same as Figure 4, but for mid September 1997.

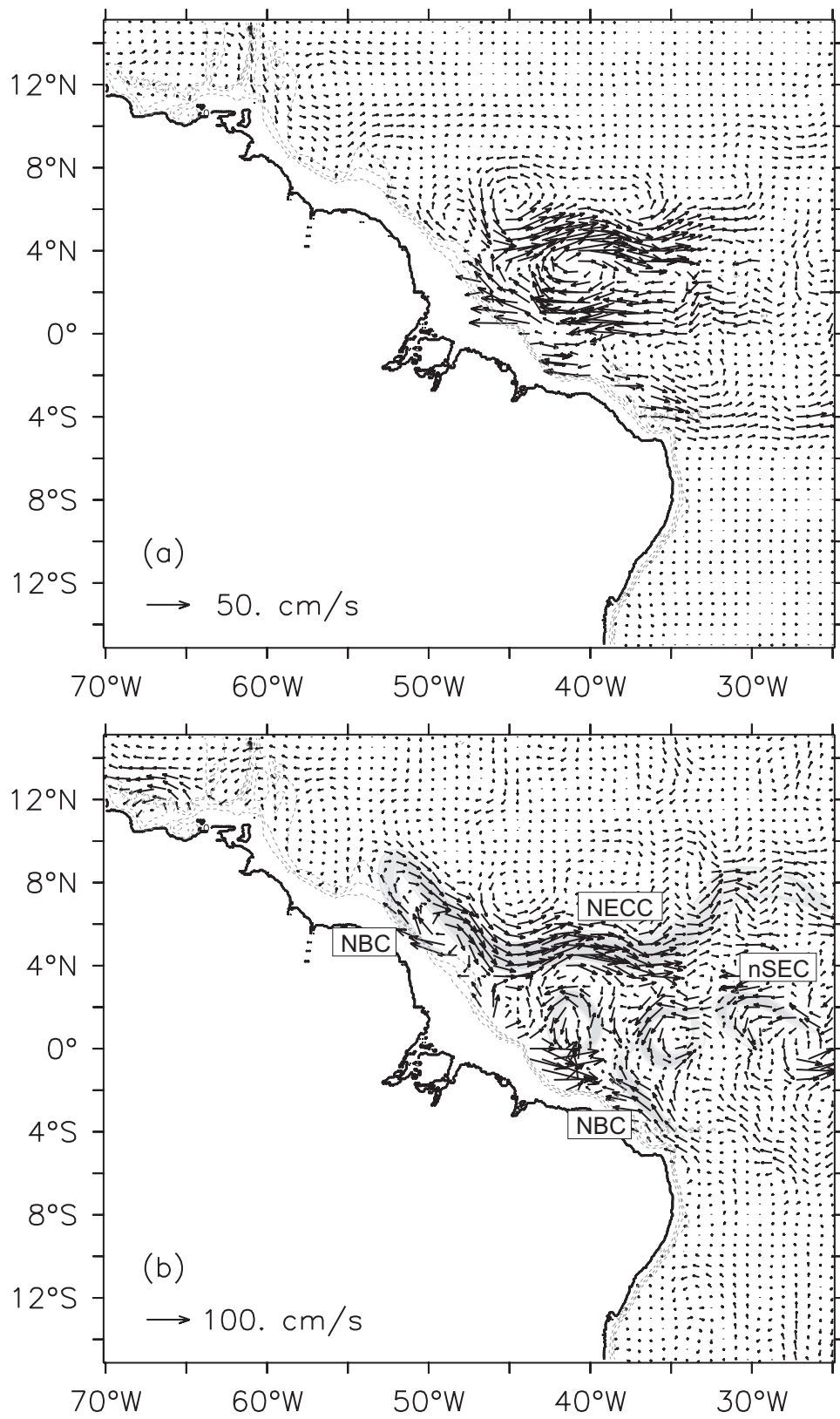


Figure 8. Same as Figure 4, but for mid November 1997.

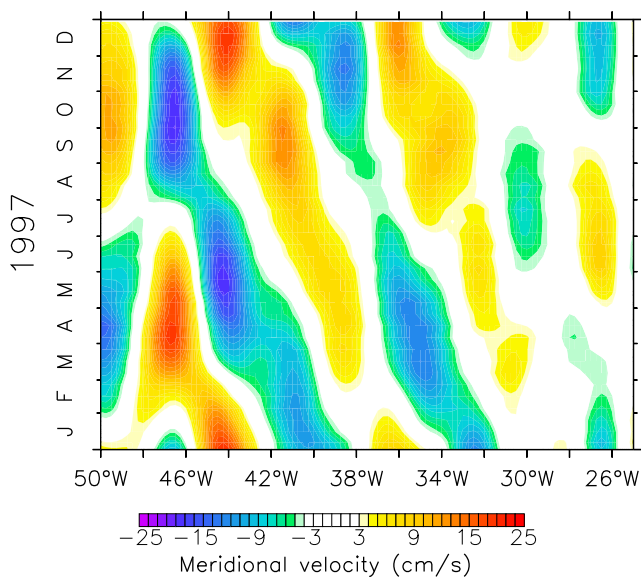


Figure 9. Time-longitude plot for the seasonal march of the meridional velocity at the NECC core at 5°N. It clearly shows the slow westward propagation of the three meanders of the NECC west of 35°W.

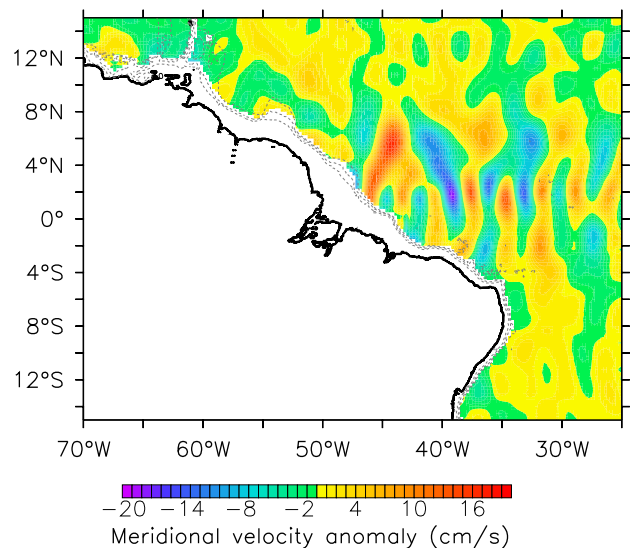


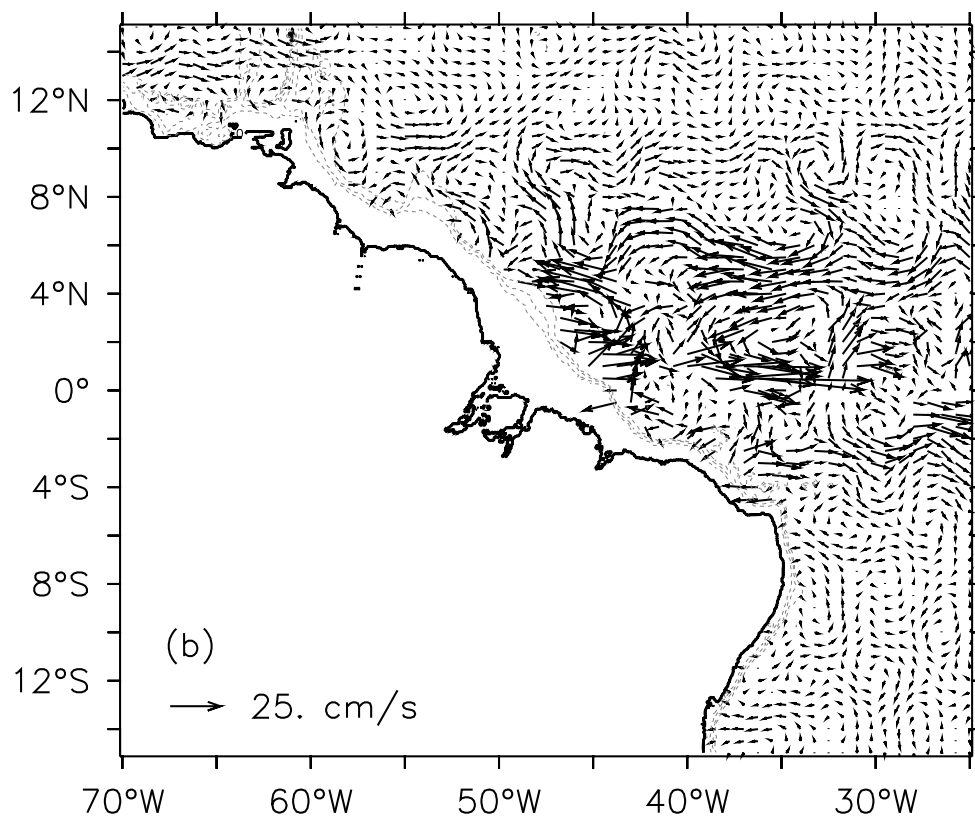
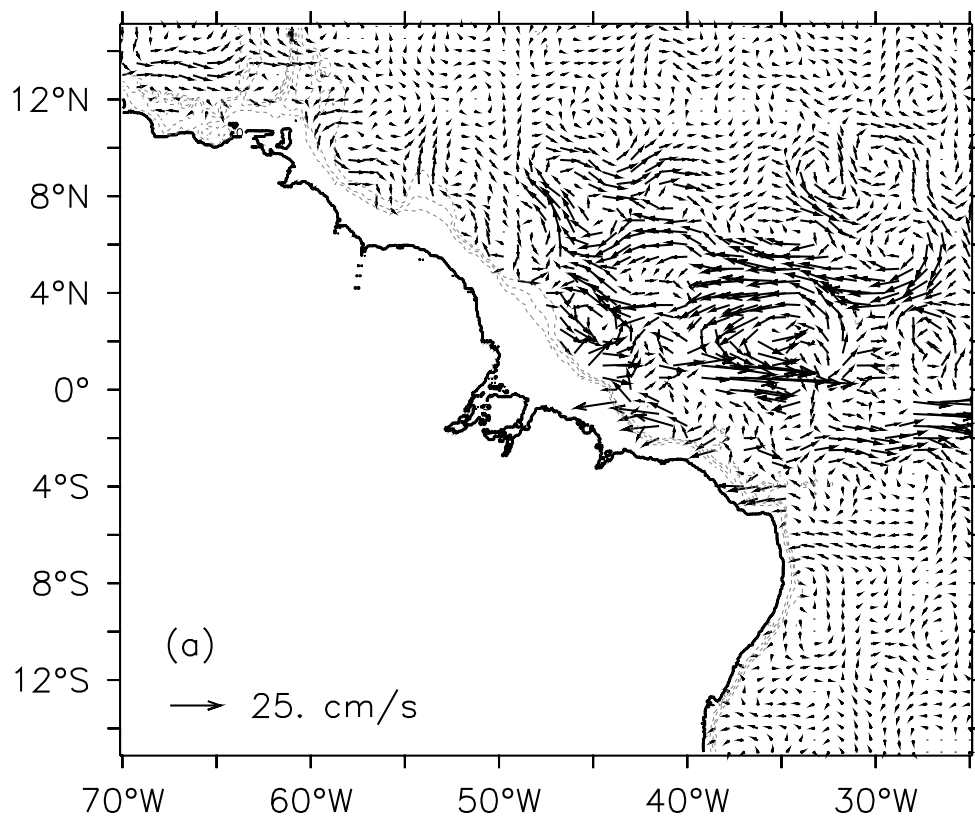
Figure 10. Meridional velocity anomaly plot for the annual cycle in mid Jan 1997. Two distinct wave patterns are seen: a trapped equatorial wave with maxima at 2°N and 2°S, and another one with maxima near 5°N.

6.4. Interannual variability

The interannual flow anomalies in the contrasting years of 1995 and 1996 is shown here to illustrate interannual variability in the upper ocean circulation. Since there is a considerable annual modulation, we choose two months (September and November) in 1995 and one month (November) in 1996 as illustrative of this contrast.

During August-September in 1995, when the NECC seasonal peak occurs, a weaker southern core and a strong northern core of the NECC are observed (Figure 11a). To better illustrate the weak perturbations in the southern hemisphere we also show the condition during November 1995 (Figure 11b). The cSEC is weakened by an eastward broad perturbation. An eddy resembling the one described by Silveira *et al.* (1994), obtained from analysis of hydrographic data, is also detected, together with a westward perturbation at 14°S. These signatures are weak and can hardly be observed in the velocity fields of Figure 11, although can be clearly seen in the current intensity/direction maps (not shown here).

The situation is exactly the opposite in 1996, both for the September and November patterns. In 1996, the main core of the NECC is at 5°N and is more intensified during the whole year, as illustrated in the September 1996 interannual anomaly pattern (Figure 11c). Finally, as a illustration of the possibly decadal modulation of the biennial anomaly in the circulation field, we show the evolution of the zonal current at the core of the NECC at 5°N (Figure 11d). We see that while in 1995 the main core of the NECC was strongly weakened, during 1996 it became strongly intensified. We notice that the biennial variability is somewhat damped in the succeeding years. The opposite is observed happens around 8°N, which is consistent with previous results (Arnault *et al.*, 1999, their Figure 11d) .



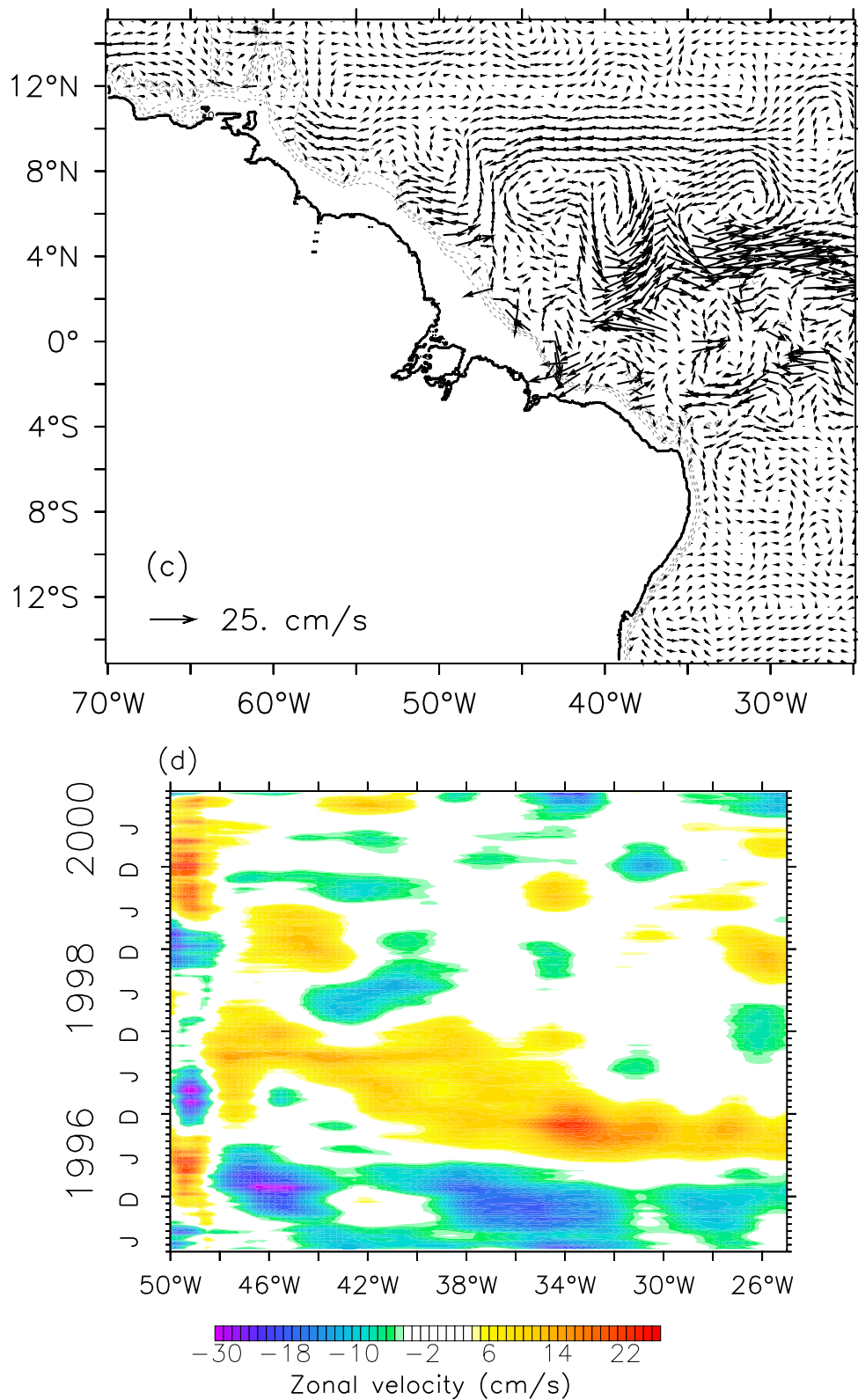


Figure 11. Interannual anomaly circulation fields in September 1995 (a), November 1995 (b), September 1996 (c) and the time-longitude diagram at 5°N for the zonal velocity, the southern core of the NECC (d). In (a) and (b) the northern core of the NECC and the EUC are more intense, and the cSEC is weaker, with the opposite situation in 1996, as exemplified for the main NECC core in (c).

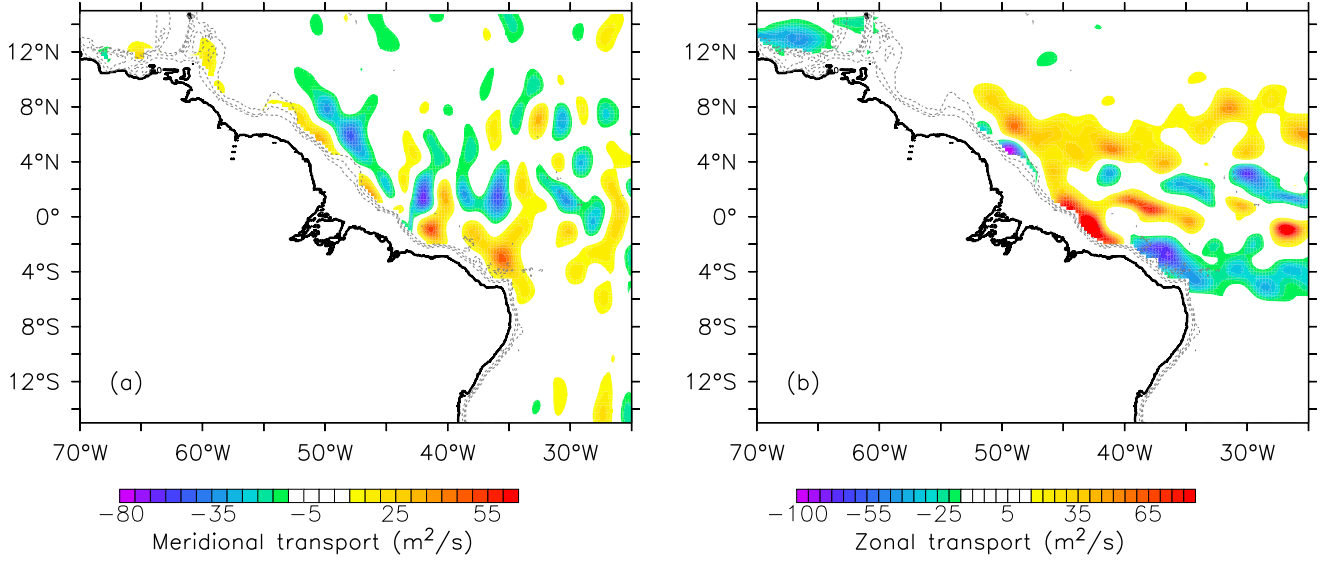


Figure 12. Multi-annual (1995-2000) average meridional transport field as in unit of distance in longitude ($Ty(x)$) (a), and the same for the zonal transport field in units of distance in latitude ($Tx(y)$) (b).

7. INTER-HEMISPHERIC TRANSPORTS AND TRANSPORT PATHWAYS

The multi-year averages for meridional ($Ty(x)$) and zonal transports ($Tx(y)$) calculated using equation (8a) are shown in Figures 12a and 12b. We can observe that $Ty(x)$ (Figure 12a) presents a meridionally banded structure across the Equator, predominating the transport windows from the South to the North Atlantic at 42°W, 34°W and 26°W indicating a 850 km zonal wavelength northward mean transport pattern. For $Tx(y)$ (Figure 12b), we see the well-known zonally banded structure, with the westward transport of the two branches of the SEC cut by the EUC eastward flow, and the broad NECC eastward transport. Westward flow into the Caribbean Sea is stronger near the South American shelf. Near the North Brazilian shelf, we notice the strong westward transport into the shelf south of 2°S that, due to continuity, accelerates the NBC. Between 2°S and the Equator, we see the strong change into eastward flow, which by following the same argument feeds the EUC.

The characteristics of these patterns were analyzed in the interannual period band. It was found that variability in the zonal and meridional directions have different spectral characteristics. In the case of the meridional transports, a nonlinear trend appears in the singular spectrum decomposition, suggesting a 6.8 year period, which is an harmonic of the 13 year dominant period in the SST interhemispheric gradient. The QB spectral peak is very broad in the zonal transport, but quite well defined in the meridional. This situation can be seen more clearly in the total transports at 3°N and 3°S, that were computed as a measure of the upper-layer geostrophic transports. The interannual variability is shown here added to each mean (Figures 13a and 13b). We can observe the quasi-biennial variability in these meridional transports, and a small phase difference between the interannual variability of the northern and the southern hemispheres. A phase difference has been also observed by Servain (1991) in his study of basinwide tropical Atlantic SST averages. He calculated monthly northern

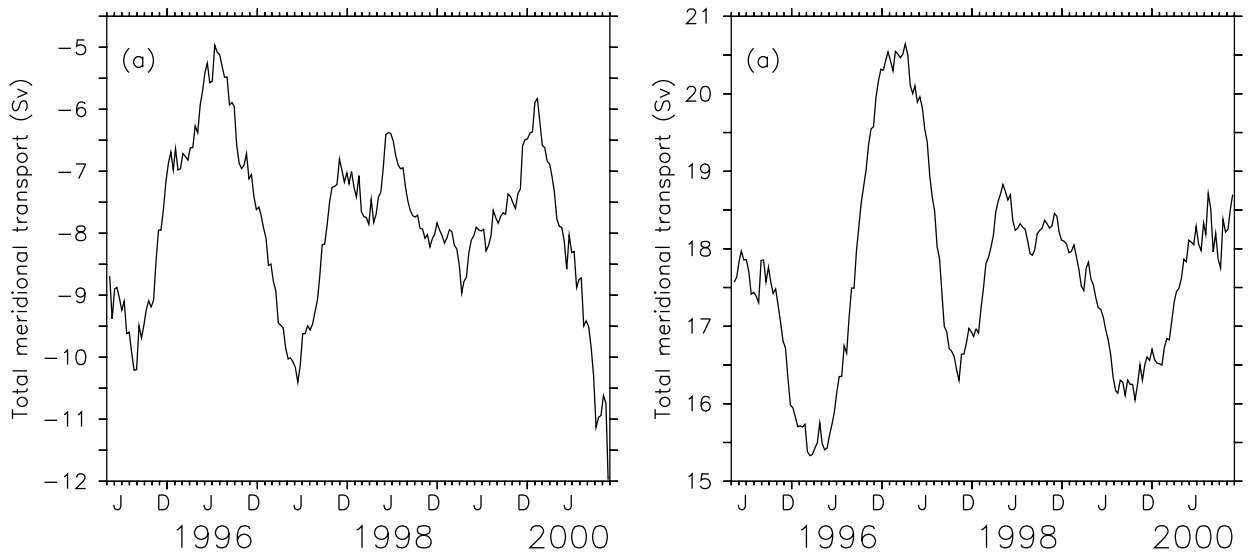


Figure 13. Total meridional transports from the western boundary to 25°W at 3°N (a) and 3°S (b). 1 Sv = $10^6 m^3 s^{-1}$.

(30°N - 5°N) and southern (5°N - 20°S) basin SST indices for the period 1964 - 1990 and noted phase differences between the two, which led him to introduce his SST dipole index. Subsequent work has shown that the mean northern hemisphere SST interannual variability spectrum and phase vary independently from the southern hemisphere counterpart, but still presenting large mean interhemispheric gradients, usually resembling a SST interhemispheric dipole (see Servain *et al.* 1998 for more details, and references therein). Our result suggests that a subsurface connection with the surface processes possibly exists, coupling a *SST dipole* type of oscillation with a STC-type vertical circulation cell.

8. SUMMARY AND CONCLUSIONS

This work documents the variability of the western equatorial Atlantic thermocline circulation and volume transports with eddy-resolving grid resolution, aiming at presenting a picture against which future model work can be tested against. Novel methods of computation were used to make possible this description and presented here for completeness:

1. Although satellite-derived circulation using of the geostrophic approximation has been used by many authors, application of this method to the equatorial ocean is less straightforward. We developed a new alternative by deriving a formulation for the computation of currents spanning the Equator. We show that the zonal geostrophic balance equation can be generalized to include the Equator using the meridional second derivatives of SSH. The derived expression is one solution of a quadratic equation in the zonal velocity, which follows directly from the shallow water equations and the equatorial scalings.
2. Since this method has not yet been fully explored, we presented a comparison with WOCE cruise data (dynamic height and ADCP current data). We also compared the SSHA grid produced for this work with data from the PIRATA moorings. Our results

suggest that altimeter-derived currents in the equatorial western Atlantic correlate better with subsurface currents, and less with surface mixed layer currents.

3. One not very well-known feature of the high resolution Boyer-Levitus climatology is the fact that it includes both average mesoscale features and noise, which are difficult to separate. The fact that ocean climatologies may contain mesoscale features is known in the case of the South Pacific Ocean, but to our knowledge this has not been studied in the Atlantic to this date. Our altimetric study seems to confirm that some important standing mesoscale oscillating features do appear near the Equator, supporting the view that the Boyer-Levitus average mesoscale features do correspond to reality.
4. The methods used to filter out high frequency-wavenumber noise from the compound grid of SSHA added to the Boyer-Levitus-derived mean SSH, and to separate the satellite-derived flow grids into period bands, have been briefly described. The mean flow field, and the annual evolution of the thermocline circulation was presented in mid-month 10-day average patterns for the year of 1997, with the aid of the data set filtered to keep only the annual cycle. This preference in relation to the more straightforward method of climatological monthly averages is explained. The patterns thus obtained were compared to those published in other works, especially with the results of Schott and Boning (1991) at their 133 m level, with which most results are consistent. The NECC presents a 3-crest meander pattern which propagates westwards. One of the differences noticed was the slow meander propagation in the NECC main core (1.8 km/day), which in the latter work was found to be stationary, and a confirmation was the finding of a double-cored NECC.
5. Another important result is the finding that the EUC is not so continuous on the Equator in the western Atlantic. The ADCP measurements presently available as a rule show either positive or negative meridional velocities, and our altimeter-derived currents further suggests that this disrupting variability may be due to almost standing mesoscale eddies spanning the Equator. However, the absence of a continuous core of the EUC in our circulation fields may be due to dynamics and steric effects, since the EUC flow is more related to a second baroclinic mode rather than to the first (Philander, 1990), whereas our determination of the current was based on a single baroclinic mode.
6. Interannual variability of the NECC was found to be mostly in the biennial band, with a decadal modulation which decays in the 1995-2000 period. We did not find a 4-year nonlinear trend in our analysis of the 1995-2000 records, which would confirm the clear 3-4 year spectral result of Katz (1993), obtained from echosounder data. The variability south of 5°S was found to be mostly in the interannual band. The prominent anomaly feature found was a large eddy which seems to change from cyclonic to anti-cyclonic each year, centered around 10°S. However, due to the weaker currents in this region, we did not show these results in the plots present in this work for brevity.
7. One interesting finding was the presence of a quasi-standing equatorial wave pattern, which modulates spatially the interhemispheric open ocean transport pathways into three windows, and channels the northward geostrophic transport. Contrary to expectations, the thermocline waters from the South Atlantic leak into the North Atlantic up to at least 4°N through these windows. The same situation is observed in the southward flow, which is also through a number of windows. In this case, the western boundary window injecting Guyana Current/NBC retroflected waters into the EUC is also noted. This

makes the mean equatorward transports different between hemispheres, with the South Atlantic at 3°S contributing 10 Sv more than the North Atlantic at 3°N into the Equator. Part of this transport goes into the EUC, and part into the Ekman return flow, including the flow over the continental shelf, which is known to be northwestward.

8. Interannual variability of these geostrophic transports were documented. It was found that the meridional transports present an out-of-phase relation, with the South Atlantic leading the changes. As an example, in January-April 1997, the equatorward transport at 3°S was more than 20 Sv (annual cycle filtered out), while at 3°N the peak was 10 Sv in June. The study of the coupling between zonal and meridional transports is omitted here for brevity.
9. One important transport process is the one effected by NBC rings (Goni and Johns, 2001), which spread southern water masses into the north Atlantic. Although our grids are eddy-resolving, we did not determine if the filtering method used here results in seasonal and interannual circulation fields that account for the net water transport by moving eddies.

This work suggests that a study of the inter-hemispheric STC dynamics can be made based on presently available surface data obtained from space-borne instruments. However, one must keep in mind that a problem with this method is its possible underestimation of upper layer geostrophic currents in transition regions. In these regions, strong subsurface currents may appear, in spite of weak surface dynamic height or sea level gradients, which would give rise to weaker currents. Mayer *et al.* (2001) reported an investigation into this matter based on thermosteric anomalies. The effects of salinity were not included, so further investigations are needed to clarify this issue.

Investigations to better determine the nature of the open-ocean transport pathways suggested here demands the use of very high-resolution eddy-resolving ocean modeling studies, which are presently lacking. Our results also suggest that these models should incorporate parameterizations of subgrid-scale horizontal mixing with smaller eddy viscosities than usual. This would allow for less attenuation of the reflected waves with small wavelength and slow propagation velocity from the western boundary. Future work will concentrate on completing the picture given here with the use of satellite scatterometer winds, and better equations to calculate Ekman currents and Ekman pumping velocities valid also along the Equator, to get a more complete picture of the variability of the three dimensional upper ocean circulation fields.

APPENDIX: PREPARATION OF BAND-LIMITED CIRCULATION AND TRANSPORT FIELDS

As described in section 4.4 a special adaptive filtering method was used to separate the circulation and transport fields in the period bands of interest. This method was applied separately for each of the components (zonal and meridional) and can be summarized as follows:

- a. For each grid point the total time average was removed,
- b. The anomaly fields were expanded into a number of EOF's necessary to account for 99% of the total variance,
- c. The corresponding Principal Component (PC) time series of each EOF mode were then analyzed by the MSSA method and decomposed into 205 T-EOF's (Reconstructed time series components-RC's), necessary to account for 99% of the explained variance,

d. Each of the RC's from (c) were spectrally analyzed with a Yule-Walker Auto-Regressive Analysis, where the most energetic spectral peak was determined. These informations allowed us to select those RC's within the period bands of intra-seasonal (less than 150 days), semi-annual (between 150 and 240 days), the annual (between 240 and 400 days), and the interannual (more than 400 days) variations. Therefore, each PC was decomposed into 4 band-limited series,

e. Since each RC has associated with it the variance explained, selection of RC's by a criterion based on their spectra, obtained from analysis (c) and (d), permitted the sum of corresponding variances to obtain the total variance per band, and

f. The band-limited data were therefore obtained by a reconstruction using the selected PC-EOF pairs, which were then inverted back into image time series.

The method proved to be very efficient and straightforward, with the advantage of bookkeeping all of the variances involved.

Acknowledgements

We are indebted to two anonymous reviewers for constructive criticism, and to Gustavo Goni for his comments, unlimited patience, and encouragement. One of us (V.V.M.) was supported by project PD001/PCO-01 in VM Oceânica. We are also grateful to FAPESP, for support to M.L.V., during the 2001 Ocean Odyssey IAPSO conference in Mar del Plata, where this EOS book was proposed. We are also grateful to the NASA Ocean Pathfinder and WOCE Projects for making available their global data sets.

REFERENCES

- Arnault, S., Boulés, B., Gouriou, Y. and Chuchla, R. Intercomparison of the upper layer circulation of the western equatorial Atlantic Ocean: in situ and satellite data. *J. Geophys. Res.*, **104**, 21171-21194, 1999.
- Boulés, B., Gouriou, Y. and Chuchla, R. On the circulation in the upper layer of the western equatorial Atlantic. *J. Geophys. Res.*, **104**, 21151-21170, 1999.
- Boyer, T. and Levitus, S. Objective analyzes of temperature and salinity for the world ocean on a quarter-degree grid. *NOAA Atlas NESDIS 11*, U.S. Dept. of Commerce, Washington, D.C, 1997.
- Chang, P., Ji, L. and Li, H. A decadal climate variation in the tropical Atlantic Ocean from thermodynamic air-sea interactions. *Nature*, **385**, 516-518, 1997.
- Diggs, S., Kappa, J., Bartolacci, D. and Swift, J. WHP CD-ROM version 2.0. Scripps Institution of Oceanography, University of California San Diego, SIO Reference 00-11, 2000.
- Dourado, M. and Caniaux, G. Surface heat budget in an oceanic simulation using data from tropical ocean-global atmosphere coupled ocean-atmosphere response experiment. *J. Geophys. Res.*, **106**, 16623-16640, 2001.
- Garzoli, S.L. and Molinari, R.L. Ageostrophic transport in the upper layers of the tropical Atlantic Ocean. *Geophys. Res. Lett.*, **28**, 4619-4622, 2001.
- Gill, A. *Atmosphere-Ocean dynamics*. Academic Press, 662 pp, 1982.
- Goni, G.J. and Johns, W.E. A census of the north Brazil current rings observed from Topex/Poseidon Altimetry: 1992-1998. *Geophys. Res. Lett.*, **28**, 1-4, 2001.
- Halpern, D., Zlotnicki, V., Woiceshyn, P.M., Brown, O.B., Feldman, G.C., Freilich, M. H. and Wentz, F.J. An atlas of monthly mean distribution of SSMI surface wind speed,

- AVHRR sea surface temperature, TMI sea surface temperature, AMI surface wind velocity, SEAWIFS chlorophyll-a, and TOPEX/POSEIDON sea surface topography during 1998. *JPL Publication 00-08*, 101 pp, 2000.
- Holvorcem, P.R. and Vianna, M.L. Integral equation approach to tropical ocean dynamics: part II - Rossby wave scattering from the equatorial Atlantic western boundary. *J. Mar. Res.*, **50**, 33-61, 1992.
- Katz, E.J. An interannual study of the Atlantic north equatorial countercurrent. *J. Phys. Oceanogr.*, **23**, 116-123, 1993.
- Kessler, W. and McCreary, J.P. The annual wind-driven Rossby wave in the subthermocline equatorial Pacific. *J. Phys. Oceanogr.*, **23**, 1192-1207, 1993.
- Koblinski, C.J., Ray, R., Beckley, B.D., Wang, Y., Tsaoussi, L., Brenner, A. and Williamson, R. Ocean altimeter Pathfinder project - report 1: data processing handbook. *NASA/TM-1998-208605*, 55 p, 1999.
- Lagerloef, G.S.E., Mitchum, G.T., Lukas, R.B. and Niiler, P. Tropical Pacific near-surface current from altimeter, wind and drifter data. *J. Geophys. Res.*, **104**, 23313-23326, 1999.
- Larnicol, G., Ayoub, N. and Le Traon, P.Y. Major changes in Mediterranean sea level variability from 7 years of Topex/Poseidon and ERS-1/2 data. *J. Mar. Syst.*, **33-34**, 63-89, 2002.
- Lazar, A., Inui, T., Busalacchi, A.J., Malanotte-Rizzoli, P., Wang, L. and Murtugudde, R. Seasonality of the ventilation of the tropical Atlantic thermocline in a OGCM. *J. Geophys. Res.*, **107**, 18001-18017, 2002.
- Liu, Z. and Philander, S.G.H. How different wind stress patterns affect the tropical- subtropical circulations of the upper ocean. *J. Phys. Oceanogr.*, **25**, 449-462, 1994.
- Maes, C. Estimating the influence of salinity on sea level anomaly in the ocean. *Geophys. Res. Lett.*, **25**, 3551-3554, 1998.
- Malanotte-Rizzoli, P. *Modern approaches to data assimilation in ocean modeling*. Elsevier Oceanographic Series, Elsevier, Amsterdam, 455 pp, 1996.
- Malanotte-Rizzoli, P., Hedstrom, K., Arango, H. and Haidvogel, D.B. Water mass pathways between the subtropical and tropical Ocean in a climatological simulation of the north Atlantic ocean circulation. *Dyn. Atmos. Oceans*, **32**, 331-371, 2000.
- Mayer, D.A., Molinari, R.L., Baringer, M.O. and Goni, G.J. Transition regions and their role in the relationship between sea surface height and subsurface temperature structure in the Atlantic Ocean. *Geophys. Res. Lett.*, **28**, 3943-3946, 2001.
- McCarthy, M.C., Talley, L.D. and Roemmich, D. Seasonal to interannual variability from expendable bathythermograph and Topex/Poseidon altimeter data in the south Pacific subtropical gyre. *J. Geophys. Res.*, **105**, 19535-19550, 2000.
- McCreary, J.P. and Lu, P. Interaction between the subtropical and equatorial ocean circulation: the subtropical cell. *J. Phys. Oceanogr.*, **24**, 466-497, 1994.
- Mehta, V. Variability of the tropical ocean surface temperatures at decadal-multidecadal timescales: part 1. the Atlantic ocean. *J. Climate*, **11**, 2351-2375, 1998.
- Molinari, R.L., Garzoli, S.L. and Schmitt, R.W. Equatorial currents at 1000 m in the Atlantic Ocean. *Geophys. Res. Lett.*, **26**, 361-363, 1999.
- Philander, S.G. *El Niño, La Niña, and the southern oscillation*. Academic Press, N.Y., 289 pp, 1990.
- Picaut, J., Hayes, S.P. and McPhaden, M.J. Use of the geostrophic approximation to estimate

- time-varying zonal currents at the Equator. *J. Geophys. Res.*, **94**, 3228-3236, 1989.
- Picaut, J., Busalacchi, A.J., McPhaden, M.J. and Camusat, B. Validation of the geostrophic method for estimating zonal currents at the Equator from Geosat altimeter data. *J. Geophys. Res.*, **95**, 3015-3024, 1990.
- Picaut, J. and Tournier, R. Monitoring the 1979-1985 equatorial Pacific current transports with expendable bathythermograph data. *J. Geophys. Res.*, **96**, 3263-3277, 1991.
- Plaut, G. and Vautard, R. Spells of low frequency oscillations and weather regimes in the northern hemisphere. *J. Atmos. Sci.*, **51**, 210-236, 1994.
- Rebert, J.P., Donguy, J.R. and Eldin, G. Relations between sea-level, thermocline depth, heat content and dynamic height in the tropical Pacific Ocean. *J. Geophys. Res.*, **90**, 11719-11725, 1985.
- Schott, F. and Boning, C. The WOCE model in the western equatorial Atlantic: upper layer circulation. *J. Geophys. Res.*, **96**, 6993-7004, 1991.
- Segschneider, J., Balmaseda, D. and Anderson, D.L.T. Anomalous temperature and salinity variations in the tropical Atlantic: possible causes and implications for the use of altimeter data. *Geophys. Res. Lett.*, **27**, 2281-2284, 2000.
- Servain, J. Simple climatic indices for the tropical Atlantic Ocean and some applications. *J. Geophys. Res.*, **96**, 15137-15146, 1991.
- Servain, J., Busalacchi, A.J., McPhaden, M.J., Moura, A.D., Reverdin, G., Vianna, M.L. and Zebiak, S.E. A pilot research moored array in the tropical Atlantic (PIRATA). *Bull. Am. Met. Soc.*, **79**, 2019-2031, 1998.
- Silveira, I.C.A., Miranda, L.B. and Brown, W.S. On the origins of the North Brazil current. *J. Geophys. Res.*, **99**, 22501-22510, 1994.
- Vauclair, F. and du Penhoat, Y. Interannual variability of the upper layer of the tropical Atlantic from in situ data between 1979 and 1999. *Clim. Dyn.*, **17**, 527-546, 2001.
- Vossepoel, F.C., Reynolds, R.W. and Miller, L. Use of sea level observations to estimate salinity variability in the tropical Pacific. *J. Atmos. Oceanic Technol.*, **16**, 1401-1415, 1999.
- Wang, V.M. The satellite altimeter data derived mean sea surface. *Geophys. Res. Lett.*, **27**, 701-704, 2000.
- WOCE data products committee. WOCE global data: ADCP data, version 2.0, WOCE international project office, WOCE report No.171/00, Southampton, UK, 2000.
- Xie, S.P. A dynamic ocean-Atmosphere model of the tropical Atlantic decadal variability. *J. Climate*, **12**, 64-70, 1999.